



Overview of the Atmospheric Brown Cloud East Asian Regional Experiment 2005 and a study of the aerosol direct radiative forcing in east Asia

Teruyuki Nakajima,¹ Soon-Chang Yoon,² Veerabhadran Ramanathan,³ Guang-Yu Shi,⁴ Toshihiko Takemura,⁵ Akiko Higurashi,⁶ Tamio Takamura,⁷ Kazuma Aoki,⁸ Byung-Ju Sohn,² Sang-Woo Kim,² Haruo Tsuruta,¹ Nobuo Sugimoto,⁶ Atsushi Shimizu,⁶ Hiroshi Tanimoto,⁶ Yousuke Sawa,⁹ Neng-Huei Lin,¹⁰ Chung-Te Lee,¹¹ Daisuke Goto,¹ and Nick Schutgens¹

Received 25 May 2007; revised 20 November 2007; accepted 6 December 2007; published 29 December 2007.

[1] This article introduces an international regional experiment, East Asian Regional Experiment 2005 (EAREX 2005), carried out in March–April 2005 in the east Asian region, as one of the first phase regional experiments under the UNEP Atmospheric Brown Cloud (ABC) project, and discusses some outstanding features of aerosol characteristics and its direct radiative forcing in the east Asian region, with some comparison with the results obtained in another ABC early phase regional experiment, ABC Maldives Monsoon Experiment (APMEX) conducted in the south Asian region. Time series of aerosol optical thickness (AOT), single scattering albedo (SSA), aerosol extinction cross section profile and CO concentration shows that air pollutants and mineral dust were transported every 5 to 7 days in the EAREX region to produce SSA values at wavelength of 700 nm from 0.86 to 0.96 and large clear-sky shortwave forcing efficiency at 500 nm from 60 W m^{-2} to 90 W m^{-2} , though there are some unexplained inconsistencies depending on the evaluation method. The simulated whole-sky total forcing in the EAREX region is -1 to -2 W m^{-2} at TOA and -2 to -10 W m^{-2} at surface in March 2005 which is smaller in magnitude than in the APMEX region, mainly because of large cloud fraction in this region (0.70 at Gosan versus 0.51 at Hanimadhoo in the ISCCP total cloud fraction). We suggest there may be an underestimation of the forcing due to overestimation of the simulated cloudiness and aerosol scale height. On the other hand, the possible error in the simulated surface albedo may cause an overestimation of the magnitude of the forcing over the land area. We also propose simple formulae for shortwave radiative forcing to understand the role of aerosol parameters and surface condition to determine the aerosol forcing. Such simple formulae are useful to check the consistency among the observed quantities.

Citation: Nakajima, T., et al. (2007), Overview of the Atmospheric Brown Cloud East Asian Regional Experiment 2005 and a study of the aerosol direct radiative forcing in east Asia, *J. Geophys. Res.*, *112*, D24S91, doi:10.1029/2007JD009009.

1. Introduction

[2] In the last decade, there has been a strong attention to the study of atmospheric aerosols in the Asian region, partly

because this region is expected to grow rapidly causing strong air pollution and also because generated Asian aerosols can cause significant direct and indirect climate

¹Center for Climate System Research, University of Tokyo, Kashiwa, Japan.

²School of Earth and Environmental Sciences, Seoul National University, Seoul, South Korea.

³Scripps Institution of Oceanography, University of California, San Diego, La Jolla, California, USA.

⁴Institute of Atmospheric Physics, Beijing, China.

⁵Research Institute for Applied Mechanics, Kyushu University, Kasuga, Japan.

⁶Atmospheric Environment Division, National Institute for Environmental Studies, Tsukuba, Japan.

⁷Center for Environmental Remote Sensing, Chiba University, Chiba, Japan.

⁸Department of Earth Science, Faculty of Sciences, University of Toyama, Toyama, Japan.

⁹Geochemical Research Department, Meteorological Research Institute, Tsukuba, Japan.

¹⁰Department of Atmospheric Sciences, National Central University, Chungli, Taiwan.

¹¹Graduate Institute of Environmental Engineering, National Central University, Chungli, Taiwan.



Figure 1. Site map for aerosol, cloud, and radiation measurements in Asia supported by various projects: ABC (UNEP Atmospheric Brown Cloud Project), SKYNET (MEXT Sky Radiometer Network), AERONET (NASA Aerosol Robotic Network), ADEC (Japan-Sino Joint Aeolian Dust Experiment), CEOP (GEWEX Coordinated Energy and Water Cycle Observations Project), ABC-EAREX (ABC East Asian Regional Experiment), and EAST-AIRE (East Asian Study of Tropospheric Aerosols, International Regional Experiment).

forcings to change the Earth's climate on global scale. In 1990s, a considerable research investment has started in Asia bringing large-scale international and national regional experiments such as INDOEX, ACE-Asia, TRACE-P, APEX, PEACE etc for studying precursor gases, aerosol characteristics, and radiative forcing in the south and east Asian regions [Ramanathan *et al.*, 2001a, 2001b; Huebert *et al.*, 2003; Jacob *et al.*, 2003; Nakajima *et al.*, 2003; Kondo *et al.*, 2004]. These experiments found that Asian aerosols are mixture of anthropogenic air pollutants and mineral dust aerosols in the spring season of these regions causing a strong whole-sky monthly mean radiative forcing of more than -10 W m^{-2} at the surface of the regions. It has been reported that there is a strong interaction between anthropogenic air pollutants and mineral dust aerosols [Chuang *et al.*, 2003; Tang *et al.*, 2004], which may cause an enhanced absorption by aerosols through a mechanism as proposed by Clarke *et al.* [2004]. The optical properties of Asian mineral dust-enriched aerosols look much different from that of other arid regions such as that of Saharan dust plumes [Kaufman *et al.*, 2001].

[3] Around the time of these experiments, new surface networks for aerosol and radiation measurements were built in the Asian region by scientists from Asian and world's

science communities, that complemented the networks by operational agencies such as WMO GAW (Global Atmospheric Watch), WCRP BSRN (Baseline Surface Radiation Network), UNEP EANET (Acid Deposition Monitoring Network in East Asia) etc. SKYNET (MEXT Sky Radiometer Network) is a heritage of JST/CREST/APEX (Japan Science and Technology Agency/Core Research for Evolution Science and Technology/Asian Atmospheric Particle Environmental Change Studies) by the Japanese community to build a radiation network using sky radiometer and flux radiometers [Nakajima *et al.*, 2003] <http://atmos.cr.chiba-u.ac.jp/>). NASA AERONET [Holben *et al.*, 2001] also started to fill the gaps of their Sun/sky photometer network in Asia. ADEC (Japan-China joint project for studying Aeolian Dust Experiment on Climate) established Asian dust measurement sites [Mikami *et al.*, 2006]. Figure 1 shows sites of various networks including those of ABC.

[4] Under the abovementioned background, UNEP established the Atmospheric Brown Cloud (ABC) project to study aerosols and air pollution in Asia for understanding their impact to the climate, human health, agriculture, and water resources [Ramanathan and Crutzen, 2003]. There have been two first phase regional experiments, APMEX and EAREX 2005, in September to October 2004 in south

Table 1. Location and Instrumentation at the EAREX2005 Participating Sites and an EAST-AIRE Site, Xianghe^a

Sites	Location	Organizations/Programs	Instrumentation ^b			Comments
			Radiation	Aerosols	Trace Gases	
Gosan (K)	33.28°N, 126.17°E	METRI, SNU/ABC	SRL	AN	SCO	
Anmyeon (K)	36.50°N, 126.30°E	METRI/GAW, AERONET, MPLNET	SM	AN	SCO	
Gwangju (K)	35.22°N, 126.08°E	GIST/AERONET	lidar	MOUDI		
Cape-Hedo (J)	26.87°N, 128.25°E	NIES/ABC, EANET, SKYNET, NIES-LidarNet	SRL	AN	SCO	
Amami-Oshima (J)	28.44°N, 127.40°E	MEXT/ABC, SKYNET, NIES-LidarNet	SRL	AN	SCO	closed in June 2005
Fukuejima (J)	32.75°N, 128.68°E	RIHN/SKYNET, NIES-LidarNet	SRL	AN	SCO	
Minamitorishima (J)	24.30°N, 153.97°E	JMA/GAW, SKYNET	SM	Sun photometer	SCO	
Miyakojima (J)	24.72°N, 125.32°E	JMA/ADEC, SKYNET	SRL	AN		
Cape Ochi-ishi (J)	43.15°N, 145.50°E	NIES/GAW		SM	SCO	
Hateruma Island (J)	24.05°N, 123.80°E	NIES/GAW		SM	SCO	
Hefei (C)	31.90°N, 117.17°E	IOFM, IAP; SKYNET, NIES-LidarNet	SRL	AN		
Xianghe (C)	39.75°N, 116.97°E	EAST-AIRE, AERONET, MPLNET	SRL	AN	O ₃	
Hok Tsui RAMS (HK)	22.22°N, 114.25°E	HKPU			CO, O ₃	
Phimai (T)	15.18°N, 102.05°E	CHLU/ABC, SKYNET, AERONET, NIES-LidarNet	SRL	AN	CO, O ₃	
Lu-Lin, Mt. (T)	23.47°N, 120.87°E	NCU/GAW		SM	CO	
Wan-Li area (T)						
Wan-Li CAQS	25.18°N, 121.68°E	TEPA		SM	SCO	rainwater collectors
An-Bo MAQS	25.18°N, 121.52°E	TEPA		PM10	SCO	rainwater collectors
Sie-Meng Site	25.28°N, 121.58°E	TEPA		SM		
Bamboo Mt. Site	25.18°N, 121.52°E	TEPA				cloud and rain collectors
KISANG 2000 R/V	–	KMA research vessel		SM		cloud and rain collectors

^aSite regions are defined as follows: C, China; HK, Hong Kong; J, Japan; K, Korea; T, Taiwan. Organization names are defined as follows: CHLU, Chulalongkorn University, Thailand; GIST, Gwangju Institute of Science and Technology, Korea; HKPU, Hong Kong Polytechnic University; IAP, Institute of Atmospheric Physics, China; IOFM, Anhui Institute of Optics and Fine Mechanics; JMA, Japan Meteorological Agency; KMA, Korean Meteorological Administration; METRI, KMA Meteorological Research Institute; MEXT, Ministry of Education, Culture, Sports, Science and Technology, Japan; NCU, National Central University, Taiwan; NIES, National Institute for Environmental Studies, Japan; RIHN, Research Institute for Humanity and Nature, Japan; SNU, Seoul National University, Korea; TEPA, Taiwan Environmental Protection Administration. Program names are defined as follows: ABC, UNEP Atmospheric Brown Cloud Project; ACE-Asia, IGAC Aerosol Characterization Experiment in Asian Region; ADEC, Japan-Sino Joint Aeolian Dust Experiment; AERONET, NASA Aerosol Robotic Network; MPLNET, NASA Micro-Pulse Lidar Network; EANET, UNEP Acid Deposition Monitoring Network in East Asia; EAST-AIRE, East Asian Study of Troposphere Aerosols, International Regional Experiment; GAW, WMO Global Atmospheric Watch; MPLNET, NASA Micro-Pulse Lidar Network; SKYNET, MEXT Sky Radiometer Network. Instrument names are defined as follows: MOUDI, Microorifice Uniform Deposit Impactor.

^b“SM” means that a standard measurement is carried out. For radiation measurements, “SRL” means include sky radiometer and lidar. For aerosol measurements, “AN” means include aetholometer and nephelometer. For trace gas measurements, “SCO” means include SO₂, CO, and O₃. More detailed information on instrumentation is shown by Nakajima and Yoon [2005].

Asia and March–April 2005 in east Asia, respectively. In this paper we introduce EAREX 2005 and discuss how the radiation budget is determined by the aerosol characteristics as observed and model-simulated in this region. APMEX results will be presented by Ramanathan *et al.* [2007].

2. EAREX 2005 Experiment

[5] The East Asian Regional Experiment 2005 (EAREX 2005) of the UNEP/ABC project was organized and conducted from March to April 2005 by scientists from east Asian countries and others [Nakajima and Yoon, 2005] <http://ABC-Gosan.snu.ac.kr/>, <http://www-abc-asia.ucsd.edu>) with the ABC supersite at Gosan, Korea, and other sites as shown in Figure 1 mostly in the East China Sea area. The earlier phase regional experiment preceding to EAREX 2005 was the ABC Maldives Monsoon Experiment

(APMEX) conducted from 1 October to 15 November 2004 in the south Asian region with another ABC supersite at Hanimaadhoo, Maldives. These two regions have large emission sources of anthropogenic aerosols and gases with largely different climates and weather conditions. APMEX and EAREX targeted detailed study of aerosol characterization in Monsoon transition periods in fall and spring seasons in these regions. Especially the EAREX 2005 region in the spring season is frequently covered by Asian yellow sand particles called Huang-sha (in Chinese) or Kosa (in Japanese). The dust particles are transported from deserts and arid regions in the Eurasian Continent by low-pressure systems which also push air pollutants out from the continent to the downstream area including Korea and Japan as simulated by chemical transport models [Takemura *et al.*, 2003; Uno *et al.*, 2003b, 2004]. Therefore the temporal variation, vertical stratification and properties of aerosols

are complicated in the EAREX region during this season. The purpose of the EAREX 2005 campaign is (1) intercalibration of instruments which are used at each site distributed in the EAREX region for long-term monitoring and (2) study of pollutant transportation and modification process, aerosol physical, chemical, and radiative characteristics, and pollution effects to the Earth's radiation budget and climate. For the intercalibration, scientists brought their instruments to the Gosan supersite during the Intensive Field Observation (IFO) period from 7 to 25 March to conduct parallel operation of instruments for comparison. In a similar period, IFO of the East Asian Study of Tropospheric Aerosols: an International Regional Experiment (EAST-AIRE 2005) was conducted at the Xianghe and Tai Lake sites, China [Z. Li *et al.*, 2007].

[6] Table 1 lists observation sites participating in EAREX 2005 with their instrumentation. It is found that after INDOEX and ACE-Asia, the Asian region has been covered by fairly good instruments for physical, chemical, and radiative measurements of atmospheric constituents, though single particle measurement instruments are still only available at large-scale sites, such as Haminadhoo [Ramana and Ramanathan, 2006; Stone *et al.*, 2007], Gosan, and Hedo [Miyazaki *et al.*, 2007]. In the IFO period of EAREX 2005, participants brought their instruments to the GOSAN supersite to perform the science campaign measurements and intercomparison programs as listed in Tables 2 and 3. Ozone concentration intercalibration measurements were done at the Gosan site by participants from Japan, Korea, Hong Kong and Taiwan in order to trace their calibration back to the Standard Reference Photometer (SRP) 35, built by the National Institute of Standards and Technology (USA) and maintained by the National Institute for Environmental Studies (Japan) [Tanimoto *et al.*, 2007a]. The assessment was expanded to measurement networks contributing to the World Meteorological Organization's Global Atmospheric Watch (WMO/GAW) program as part of off-site comparisons, and excellent agreement was achieved in the range of -0.5% to $+0.7\%$ for sensitivity, and -0.5 nmol/mol to 0.0 nmol/mol for the zero intercept. Carbon monoxide intercomparison was also performed by the same groups [Tanimoto *et al.*, 2007b]. Three nondispersive infrared absorption (NDIR) instruments from Japan, Korea, and Hong Kong showed an agreement in ambient air measurements within 5% at the maximum concentration of 1000 ppbv. They also found that results of an NDIR instrument agreed fairly well with a gas chromatograph/reduction gas detector (GC/RGD) measurements with 1-h time resolution. However, a comparison of gas standards revealed difficulties in preparing accurate and stable CO standard gases. Direct and global solar radiative fluxes comparison was performed with Kipp & Zonen pyrliometer and pyranometer [Uchiyama *et al.*, 2007]. It is suggested that 0.3% accuracy was retained through transfer of calibration constants from WMO regional standards (RA-II) of JMA (Japan Meteorological Agency) which have been regularly calibrated to the World Standard Group of the WRC (World Radiation Center). Pyranometer's accuracy was estimated as $\pm 1\%$. In the EAREX 2005 we also made intercomparison of compact lidar systems and Sun/sky photometers, which are getting popular in the Asian region, but have not been well intercalibrated in a systematic way. Overall mean relative

difference of the range-corrected raw lidar signals between SNU-MPL and NIES compact lidar systems was estimated as less than 8% (S.-C. Yoon *et al.*, Ground-based Mie-scattering lidar measurements of aerosol extinction profiles during ABC-EAREX 2005: Comparisons of instruments and inversion algorithms, submitted to *Journal of the Meteorological Society of Japan*, 2007). End to end difference including difference in signal processing algorithms was within a bias difference of 0.0086 km^{-1} and a mean deviation of 11.6% in their aerosol extinction profiles between the two lidar systems. Aerosol optical thicknesses (AOT) obtained from CIMEL 318-2 Sun/sky photometer and PREDE POM01 sky radiometer agreed with each other with differences less than 0.02.

[7] It should be noted that the EAREX region has a fairly dense network coverage of single wavelength nonpolarization MPL lidars or dual wavelength polarization NIES (National Institute of Environmental Studies, Japan) lidars [Won *et al.*, 2004; Sugimoto and Lee, 2006; Hayasaka *et al.*, 2007]. Figure 2 shows time series of vertical profiles of the aerosol extinction coefficient from lidars at wavelength of $\lambda = 532 \text{ nm}$ and time series of the surface CO concentration [Sawa *et al.*, 2007; C. Li *et al.*, 2007] at sites inland and in outflow regions of EAREX and EAST-AIRE during March 2005. Figure 2 shows periodic loading of surface CO concentration and aerosols up to 5 km height every 5 to 7 day intervals. There is a correlation among data of different sites with a systematic time lag from northwest to southeast directions indicating the time series is strongly affected by advection of atmospheric constituents from emission areas by low-pressure systems propagating with westerlies. The temporal evolution of the CO concentration at Xianghe and that of lidar extinction coefficient at Beijing is very similar with each other. At Gosan there were CO concentration peaks on 11, 17, 22, and 31 March with other minor peaks. The lidar time series shows a similar pattern, but is difficult to make a detailed comparison because of frequent intermittent breaks by rain. The time lag between Xianghe and Gosan events vary from one day to three days in the EAREX 2005 IFO period. The event timing among the three outflow region sites, Gosan, Fukue, and Amami, are very similar to each other, but some peaks are not present at the Amami site as discussed by Sawa *et al.* [2007] with their detailed model simulations. According to Uno *et al.* [2001], the transit time for dust particles from Shandon Peninsula to Tokyo can get as long as 3 days when a slow moving cutoff low-pressure system is established.

[8] We schematically illustrate in Figure 3 the event features measured by several instruments located at Gosan during the IFO period to characterize the air mass of the Gosan site. In Figure 3 the width and height of bars schematically indicate the duration and the magnitude of surface concentrations and lidar echo in the events. The ratio of PM10 and PM2.5 shows there were four mineral dust outbreaks during the period on 13, 18, 24, and 29 March. There is a tendency that gaseous constituents, sulfate and OC increase before the dust event starts. Uno *et al.* [2003a] reported similar differences in the time series of black carbon (BC), sulfate and dust concentration in their comparison of model-simulated time series with observed one. Their model simulation suggests that low-pressure systems draw out polluted air masses out over the populated region

Table 2. Instrumentation at the Gosan Supersite^a

Measurement/Instrument	Group
<i>Aerosol Measurement</i>	
PM1.0/PM1.0 sampler	GIST
PM2.5/PM2.5 cyclone and denuder filter pack system	NIER
PM2.5/PM2.5 continuous ion monitor system	NIER
PM2.5 EC/OC/semicontinuous OC/EC field instrument	GIST, NIER
PM2.5 EC/OC/continuous carbon monitor system	NIER
PM10 and PM2.5 samplers	University of Wisconsin, GIST, NIER
Black carbon/aethalometer	GIST, University of Tokyo, SIO
Scattering coefficient/nephelometer	GIST, NIER, KIST, SIO
Scanning mobility particle sizer (SMPS)	NIER, Yonsei University, University of Tokyo
Aerodynamic particle sizer (APS)	NIER
Cascade impactor	NIER
Microorifice uniform deposit impactor (MOUDI)	KIST, Yonsei University and SNU
Optical particle counter (OPC)	University of Tokyo, METRI
Particle mass/continuous particle mass concentration monitor system	NIER
Continuous online ion monitoring	GIST
Condensation particle counter (CPC)	Yonsei University, University of Tokyo
TSP (ion and metal)/high-volume tape sampler	Cheju National University
TSP (element)/high-volume air sampler	New Mexico State University
TSP (organic)/high-volume air sampler	METRI, Hokkaido University
TSP (metal)/high-volume air sampler	KORDI
Ions/particle-into-liquid-sampler (PILS) IC system	University of Tokyo
<i>Gas Measurement</i>	
O3/CO instruments	HKPU, NIES/MRI/NIAES, NCU
VOCS/canisters	KIST, HKPU
CO, O3, SO2, NOx gas analyzer	GIST, KMOE, SNU/HUFS/KU
HONO/HONO measurement system	GIST, SNU/HUFS/KU
Radon	Cheju University, SNU/HUFS/KU, METRI (ANSTO)
DMS, HNO3, PAN, Noy, H2O2, ROOH	SNU/HUFS/KU
<i>Radiation Measurement</i>	
Aerosol profile/lidar	
Dual-wavelength compact lidar	NIES
MPL	SNU (MPLNET)
Global and diffuse irradiance/pyranometer	
Kipp & Zonen CM22	MRI, CEReS, RIHN
Kipp & Zonen CM21	SNU, SIO
EKO	METRI/KMA
Direct irradiance/pyrheliometer	
Kipp & Zonen CH1	SNU, MRI, CEReS
EKO Shadowband	METRI/KMA
Global or diffuse flux/pyrgeometer	
Kipp & Zonen CG3	CEReS, SNU
Kipp & Zonen CG4	SIO
EKO	METRI/KMA
AOT and size distribution/sky radiometer	
PREDE sky radiometer	METRI/KMA, SNU (SKYNET)
PREDE i-sky radiometer	CEReS
Cimel Sun/sky photometer	SNU (AERONET)
Multifilter rotating shadowband radiometer (MFRSR)	Yonsei University
Other types of radiometers	
Grating Sun photometer (PREDE)	CEReS
Grating spectrometer (ASD)	SIO
MW radiometer	METRI/KMA
FT-IR, EKO UV-B	Kyungbuk University

^aLocation is (33°17'N, 126°10'E), altitude is 56 m above sea level. Managing organizations are METRI/KMA and SNU. Acronyms are as follows: ANSTO, Australian Nuclear Science and Technology Organization; CEReS, Center for Environmental Remote Sensing; HUFS, Hankuk University for Foreign Studies; KIST, Korean Institute of Science and Technology; KORDI, Korea Ocean Research and Development Institute; KMOE, Ministry of Environment of the Republic of Korea; KU, Korea University; MRI, JMA Meteorological Research Institute; NIAES, National Institute for Agro-Environmental Sciences; NIER, National Institute for Environmental Research, Korea; SIO, Scripps Institute of Oceanography. Refer to Table 1 and Figure 1 for other acronyms.

of China in front of the mineral dust plume from the arid areas of inland China with various transportation speeds depending on the pressure regime. Another point to be noted in Figure 3 is that the duration of lidar events was much longer than that of surface particle events indicating lidar can detect airborne fine particles of long residential time existing in high altitudes.

[9] In order to study the long-term variability of the atmospheric turbidity in the experimental region, we show in Figure 4 monthly mean aerosol optical thicknesses at 550 nm (AOT550) as a function of years from January 2004 at Gosan and Fukue sites and at the Amami site obtained by four different evaluation methods, i.e., surface sky radiometry [Nakajima *et al.*, 1996], two TERRA/MODIS remote

Table 3. Intercomparison Programs in the EAREX 2005

Comparison	Instruments (Groups)
Surface O ₃	TEI 49CPS; Dylec 1100 (NIES, MRI, NIAES); TEI 49C (SNU, HUFU, KU); TEI 49C (HKPU); Ecotech 9810 (Taiwan)
Surface CO	Horiba, APMA-360 (NIES, MRI, NIAES); TEI, 48C (SNU, HUFU, KU)
Global solar radiation	Kipp & Zonen CM21 (CCSR, CEReS, SNU); CM22 (MRI)
Direct solar radiation	Kipp & Zonen CH1 (MRI, CEReS)
Lidar retrieval	NIES-compact lidar ^a (NIES); SNU MPL lidar ^b (SNU)
Sun/sky photometry	CIMEL 318-2 (SNU); PREDE POM-01 (SNU, METRI, CEReS)

^aNIES compact lidar: 532 nm and 1064 nm, backscattering intensity and depolarization ratio; <http://www-lidar.nies.go.jp/>.

^bMPL lidar: 524 nm, backscattering intensity; <http://mplnet.gsfc.nasa.gov/>.

sensing methods by NASA [Kaufman *et al.*, 2002] and by the four channel algorithm of Higurashi and Nakajima [2002], and the SPRINTARS aerosol and radiation model implemented in the CCSR (Center for Climate System Research, The University of Tokyo)-NIES (National Institute of Environmental Studies, Japan)/AGCM (Atmospheric General Circulation Model) with resolution of T42L20 [Takemura *et al.*, 2000, 2002, 2003]. NCEP objective analysis data of each day in the simulation periods were used to nudge the meteorological fields in the model. As for the sky radiometer data we used data from Fukue near Gosan (a distance of 200 km), because there is no multiyear data at Gosan in this period. It is found that the AOT values from the two satellite methods are similar to each other with root mean square deviation (*rmsd*) of 0.05, though it

exceeds 0.1 in some cases, and show similar long-term variations as the surface observations. Large AOT550 values in the spring season are detected by all four methods, though surface sky radiometry gives slightly smaller values than satellite values by about 0.1. Satellite values may be overestimated because of small-scale invisible clouds. Such subpixel clouds tend to be misjudged as sea salt aerosols over ocean in passive remote sensing [Kaufman *et al.*, 2002]. This point is also suggested by the fact that large differences appear when error bars of sky radiometer data are large. The Amami site tends to have small clouds generated by a hill near the site depending on the wind direction. Despite of this difference, all the four methods show that the aerosol loading in the March–April season of 2005 was less than that of 2004 in the Amami region,

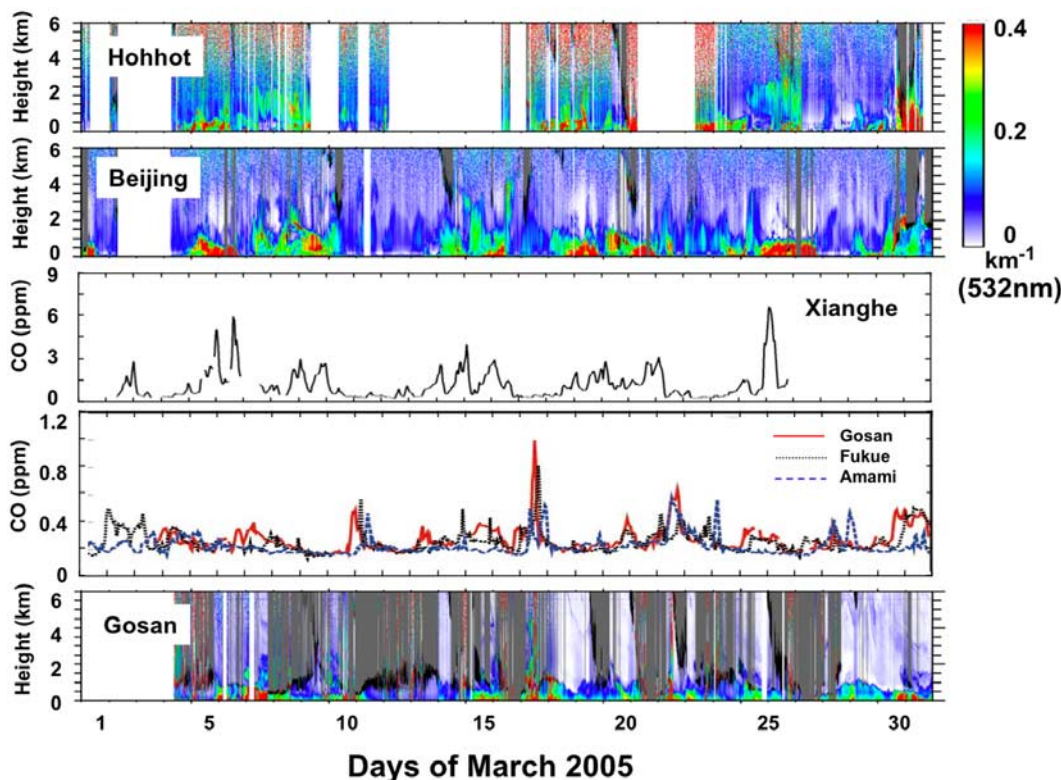


Figure 2. Time series of lidar-derived extinction cross section profiles ($\lambda = 532$ nm) at Hohhot (111.4°E, 40.9°N), Beijing, and Gosan and surface CO concentrations at Xianghe, Gosan, Fukuejima, and Amami-Oshima. Xianghe data are provided by C. Li *et al.* [2007]. Locations of sites other than Hohhot are listed in Table 1.

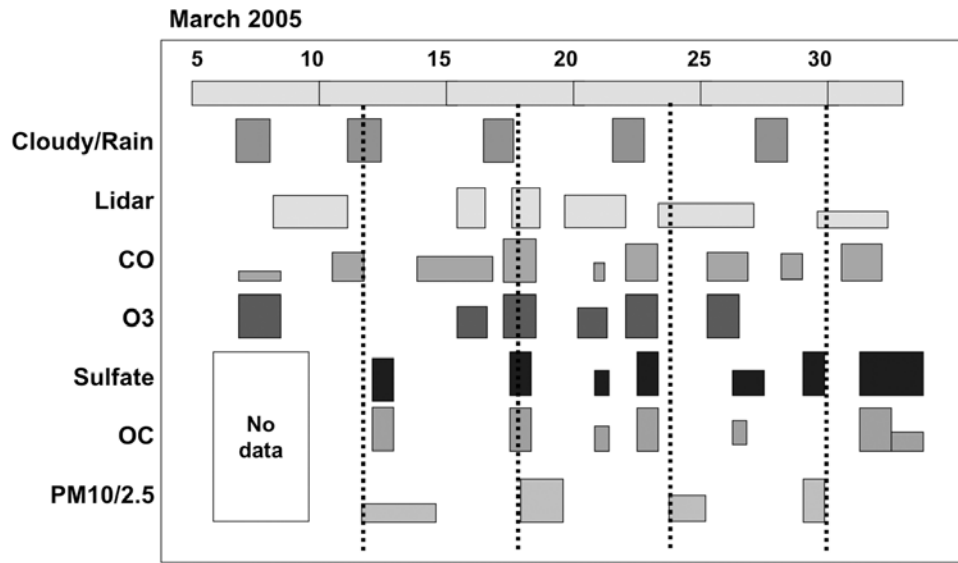


Figure 3. Schematic diagram of air mass characterization at the Gosan site in the EAREX 2005 IFO period. Width and height of bars schematically indicate the duration and the magnitude of surface concentrations and lidar echo.

whereas the loading in the Gosan region was similar to that of 2004 indicating the air mass origin is somewhat different between the two sites.

[10] The above mentioned seasonal enhancement of the aerosol loading is presented in Figure 5 in terms of monthly mean spatial distributions of AOT550 in March, April, and

May 2005 obtained from the four channel algorithm applied to TERRA/MODIS radiance data at 412 nm (band 8), 443 nm (band 9), 660 nm (band 1), and 865 nm (band 2) over ocean in the experimental area. Although the technique classifies aerosols into carbonaceous type (CRB), sulfate type (SLF), mineral dust type (DST) and sea salt type (SSL,

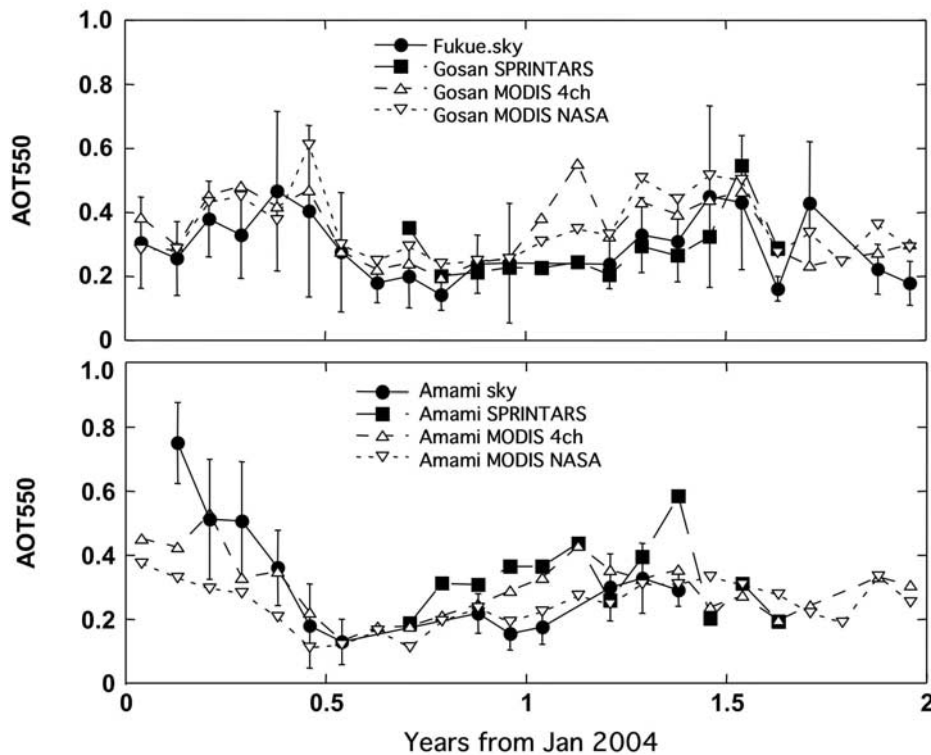


Figure 4. Time series of monthly mean AOT550 at Gosan and Amami sites as derived from different method: sky radiometry (sky), SPRINTARS model (spr), and MODIS result from four channel algorithm (4ch) and from NASA algorithm (nasa). Abscissa indicates the time in years starting from January 2004.

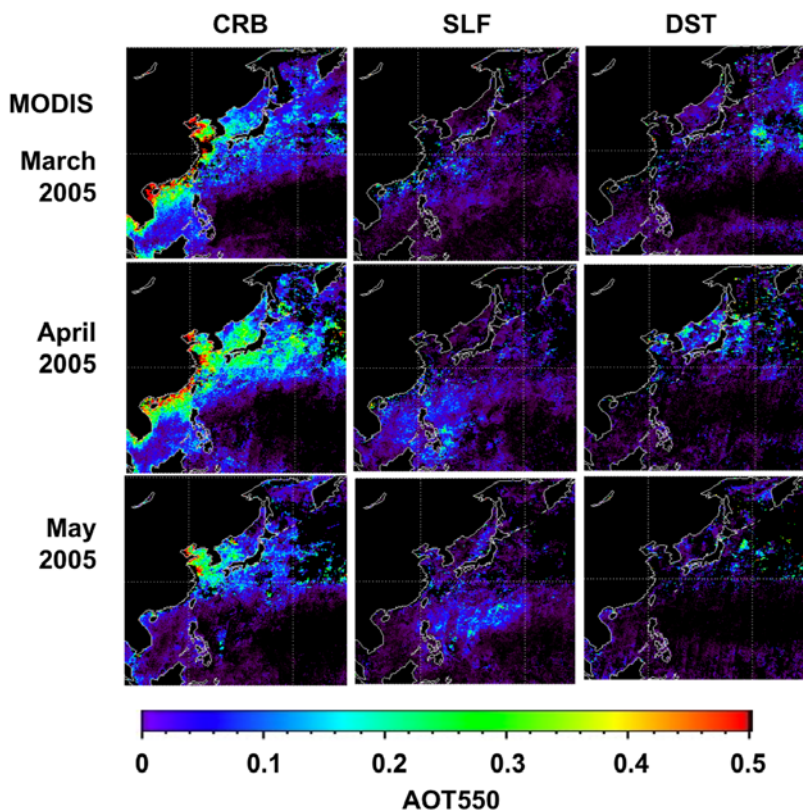


Figure 5. Monthly mean AOT550 distributions of three optically equivalent aerosol species of carbonaceous (CRB), sulfate (SLF) and mineral dust (DST) types as derived from the four-channel algorithm applying to MODIS data in March, April, and May 2005.

not shown in Figure 5), it should be recognized that these types are of optical equivalents of fine radiation-absorbing, fine nonabsorbing, coarse absorbing, and coarse nonabsorbing aerosols, respectively. Figure 5 shows that the CRB-type aerosols were dominant in the EAREX region, indicating aerosols in this region are highly absorbing and small-sized. It is also found that CRB and DST types have large AOT values in April in the region as compared to other months, that is consistent with the time series shown in Figure 4.

3. Characteristics of Aerosols

[11] In order to study the aerosol characteristics in the IFO period, we plot in Figure 6 the daily mean single scattering albedo of aerosols at 500 nm (SSA500) in the springtime of 2005 retrieved by *skyrad.pack* version 4.2 of CCSR/OpenCLASTR (<http://www.ccsr.u-tokyo.ac.jp/~clastr/>) applied to data of sky radiometers at Gosan, Fukue, Amami, and Hefei. Figure 6 shows observed SSA500 values at Gosan and Fukue are close to each other and vary in a wide range from 0.86 to 0.98. During the IFO period (day 66 to 84), the mean SSA500 was 0.97 for the Gosan. An air mass trajectory analysis indicated that large SSA values close to 1 tended to be affected by a maritime air mass without interacting with continental air mass for several days. On the other hand, SSA reduction was observed on 14 (day 73), 19, 22, and 30 March (day 89), which seems associated with the air mass events shown in Figures 2 and 3. Although not shown in a figure, this

reduction is clearly present in SSA at longer wavelengths, such as $\lambda = 865$ nm and 1020 nm of the sky radiometer, but is not so obvious in the time series of SSA500 in Figure 6. A study of SSA spectra of *Dubovik et al.* [2002] suggests that SSA865 and SSA1020 can become significantly low for urban and biomass burning aerosols with large soot fraction, while SSA500 remains high.

[12] The mean SSA500 at Amami in Figure 6 has a slightly lower value (0.95) than at Gosan and Fukue. The Hefei site usually had values less than 0.9 which can be understood by the fact that this site is located in a heavily populated area of Anhui Province, China. Study of Figure 5 suggests a slightly smaller SSA value at Amami, south of Gosan, was also affected by CRB-type aerosols from the southern part of China and Southeast Asia. *Sawa et al.* [2007] suggested by a simulated airflow analysis that CO-rich plumes covering southern sites, i.e., Miyakojima and Okinawa/Hedo, belong to a branch of the pressure system different from that covering Gosan. This point is also supported by a model simulation as shown in Figure 7. Figure 7 shows SPRINTARS-simulated monthly mean global distributions of clear-sky AOT550 and SSA550 for March 2005. SSA550 was simulated as less than 0.9 in the area close to the Korean Peninsula including Beijing, but AOT550 was simulated as lower than a tongue of large AOT550 distributed from southwestern China to the Amami-Hedo region. Thus the model result suggests that the Gosan site was under the effect of the air mass from the Beijing area, whereas the Amami-Hedo region was more

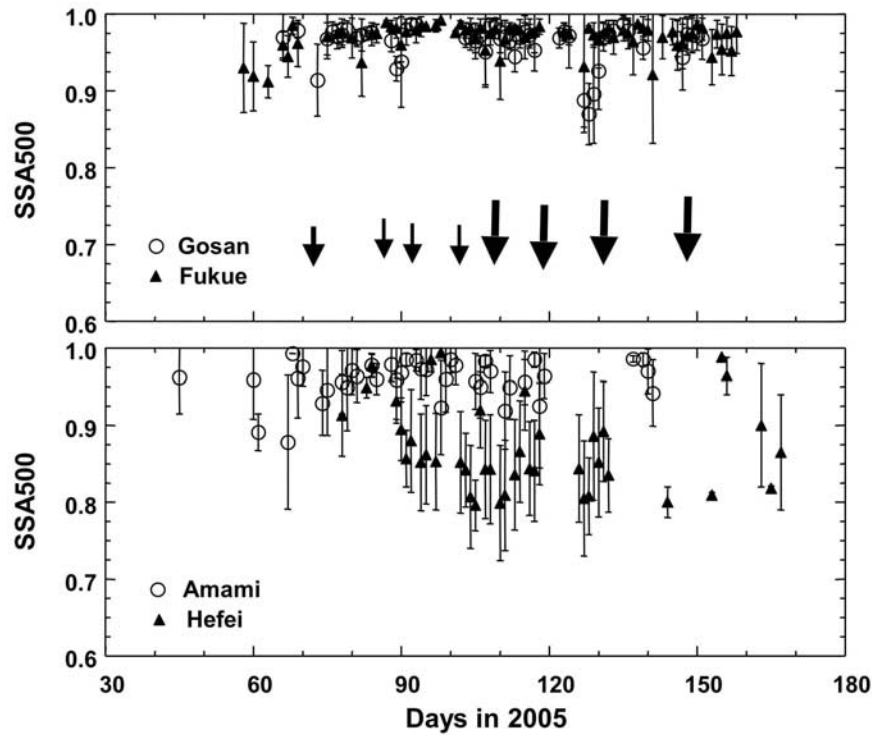


Figure 6. Time series of daily averaged SSA500 at Gosan, Amami, and Hefei sites. Abscissa indicates the time in days starting from 1 January 2005. Error bars are root mean square deviations of retrieved data on each day. Yellow sand events are also shown by arrows judged by depolarizability of lidar signals. The size of arrows schematically indicates the magnitude of the dust event.

affected by southern air masses, as consistent with the discussion related to Figures 5 and 6. Along the southern tongue of large AOT, however, the SSA value was not so strongly reduced because of significant hygroscopic growth of aerosols absorbing water vapor over the southern ocean. Hence the model simulates large SSA values at Amami than at Gosan, that is different from SSA500 values by sky radiometry at these sites. The model hygroscopic process may need an improvement.

[13] Another important parameter for determining the aerosol radiative forcing (ARF), especially for that at the top of the atmosphere (TOA), is the height of the aerosol layer. Since some of EAREX sites are equipped with a NIES dual frequency polarization lidar, it is possible to retrieve extinction cross section profiles for fine (mostly spherical secondary generation particles) and nonspherical dust particles [Sugimoto and Lee, 2006]. Figure 8 shows monthly mean profiles of nonspherical, spherical and all

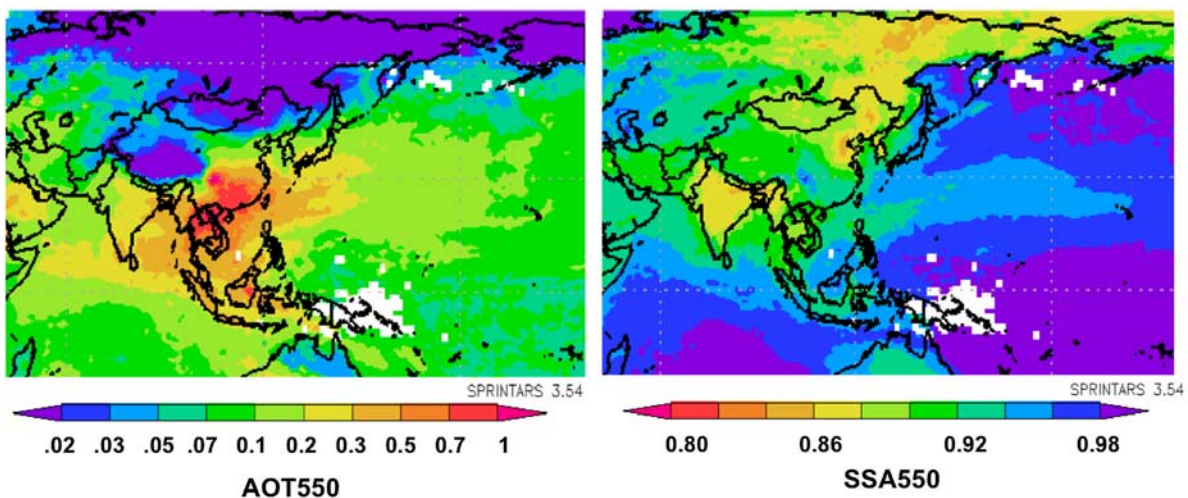


Figure 7. Monthly mean AOT500 and SSA500 distributions in the APMEX and EAREX regions simulated by the SPRINTARS model for March 2005.

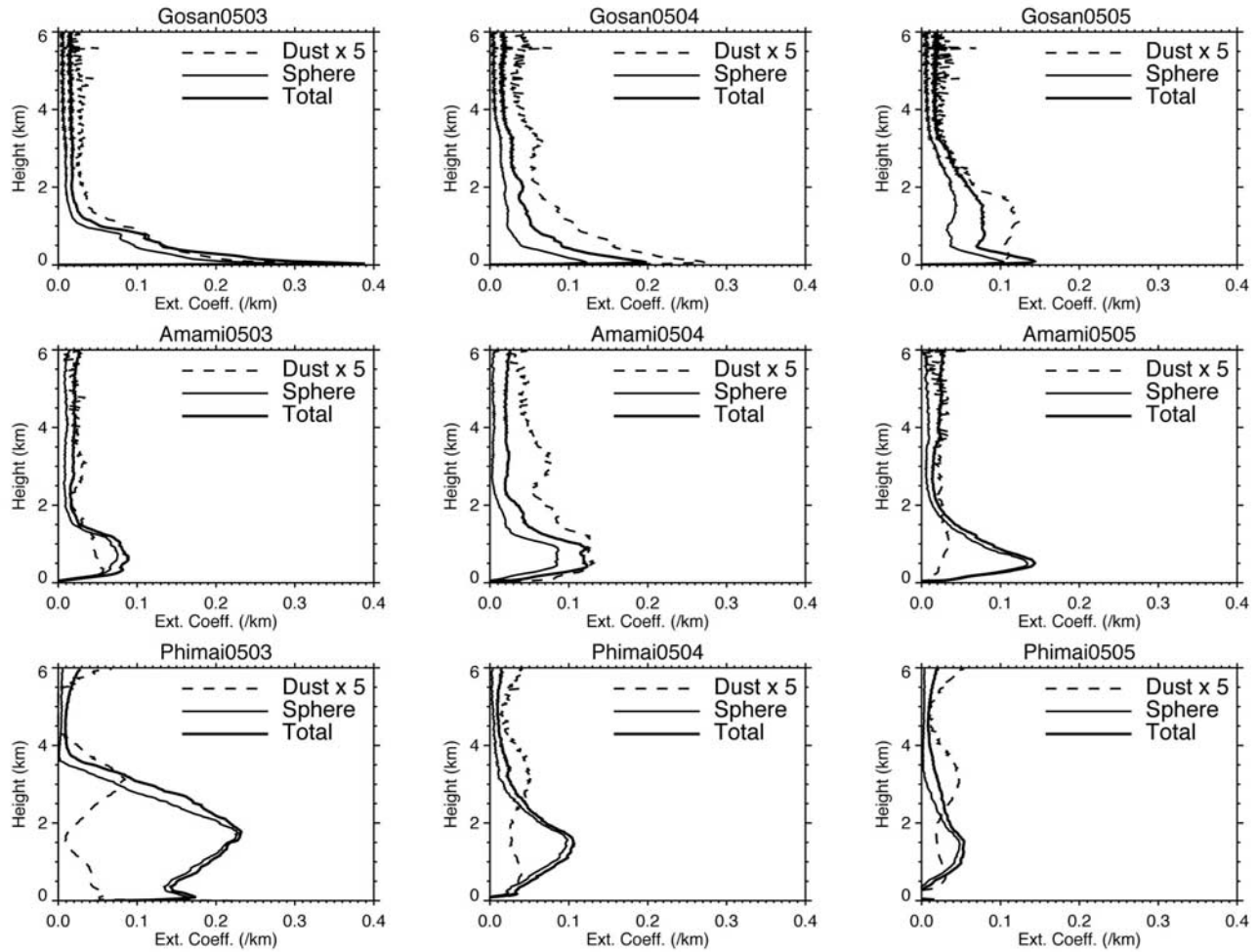


Figure 8. Vertical profiles of the aerosol extinction cross section (km^{-1}) as derived from NIES lidar observation for total, spherical (sphere) and nonspherical (dust) particles.

aerosols in March, April and May 2005 at Gosan, Amami and Phimai. At Gosan the extinction cross section profile has a sharp peak near the surface for spherical particles. Southern sites at Amami and Phimai have much broad profiles indicating aerosol particles are uplifted to high altitudes in the warm atmosphere with less stable condition. It is also possible the aerosol layer gets height during the transportation to Amami where is located in the downstream region of continental air mass. We compare in Figure 9 scale heights of aerosol extinction cross section profiles observed from lidar and model simulation. The scale height is calculated by integrating the lidar-sensed vertical profile of the extinction cross section, $e(z)$, as a function of altitude z [Hayasaka *et al.*, 2007],

$$e^{-1} = \int_h^{\infty} e(z) dz / \tau_a, \quad (1)$$

where τ_a is the aerosol optical depth.

[14] We also performed similar calculation of the simulated scale height by integrating SPRINTARS-simulated extinction cross sections in the clear-sky condition. Figure 9 shows monthly mean scale heights and *rmsd* obtained from extinction cross section profiles of all-aerosols and

dust-aerosol in March, April, and May 2005 at Gosan, Amami, and Phimai (17.15°N, 99.95°E) shown in Figure 8. Figure 9 also shows results from Taiwan National Central University (NCU; 24.97°N, 121.18°E), Toyama, Japan (36.65°N, 137.10°E), and at Hamimadhoo site in the APMEX region [Ramanathan *et al.*, 2007]. It is found from Figure 9 that the lidar data show that the scale height of mineral dust aerosols was higher than that of all aerosols as also shown by Figure 8, especially at Amami where dust particles were uplifted up to 2 km during the transportation. Larger scale height for Asian dust plumes have been reported also by Won *et al.* [2004] and others. Also it is found that the scale height of all-aerosol layers decreased almost monotonically with increasing latitude, suggesting the increasing stability of the atmosphere with latitude as one of reasons. Scale heights of simulated aerosol layers, however, are slightly larger than observed ones in the shown cases. This overestimation of the scale height of the aerosol layer may lead to underestimation of ARF at the top of the atmosphere (TOA) due to a humidity effect and a reflectivity effect of underlying cloud layers as discussed by Haywood and Boucher [2000] and Takemura *et al.* [2005]. Large error bars of the model result at Hamimadhoo reflect the rapid air mass exchange from summer regime to winter regime in

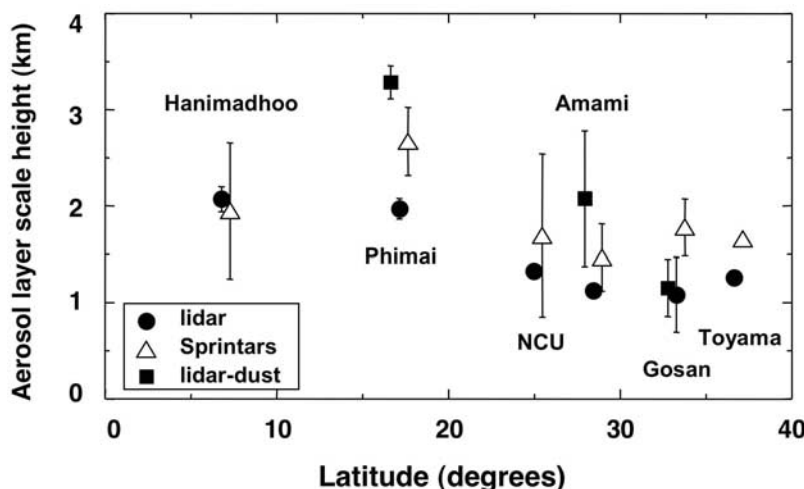


Figure 9. Scale heights of aerosol layers as derived from vertical profiles of the all-aerosol extinction cross section (circles) and dust aerosol cross section (squares) observed by lidars at several sites. Scale heights of the all-aerosol extinction cross section from model simulation are also shown (triangles). Mean values and *rmsd* of data sets are obtained from three monthly (March, April, and May 2005) mean profiles at Gosan, Amami, and Phimai shown in Figure 8; two monthly mean profiles (March and August 2005) at Taiwan National Central University (NCU; 24.97°N, 121.18°E); two profiles (September and October 2004) at Hanimadhoo; and one April profile at Toyama (36.65°N, 137.10°E). Scale heights of dust extinction cross sections are also shown at Gosan, Amami, and Phimai. Abscissa indicates the latitude of the observation sites, though small offsets are applied to avoid overlapping error bars.

September–October season [e.g., *Satheesh and Srinivasan, 2002*]. On the other hand, lidar observation tends to pick similar air mass because a fair weather condition is needed for lidar measurements.

4. Control Factors of the Direct Aerosol Radiative Forcing

[15] Leaving detailed computations of ARF to other papers of this special section, we try to understand the situation by idealized models. First we assume a simple

three component external mixture of fine particle and mineral dust aerosols. The fine particle mode is further approximated by an internal mixture of transparent aerosol (75% H_2SO_4) and soot particles by specifying the dry volume fraction of soot f_{soot} . The aerosol volume size distribution is assumed to be a sum of lognormal size distributions of these aerosol components,

$$\frac{dV}{d \ln r} = \sum_{n=1}^2 \frac{V_n}{\sqrt{2\pi}\sigma_n} \exp\left\{-\frac{1}{2}\left(\frac{\ln r - \ln r_{m,n}}{\sigma_n}\right)^2\right\} \quad (2)$$

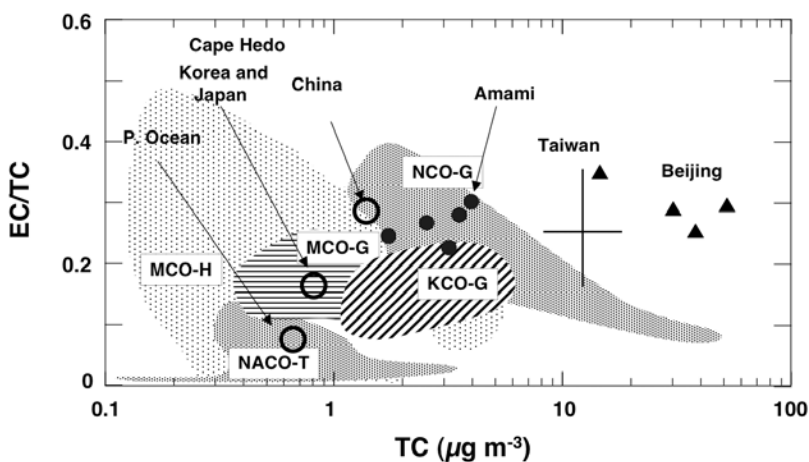


Figure 10. Relation of EC/TC ratio versus TC at sites observed in APMEX and EAREX. Data are from EAREX 2005 at Amami and Taiwan and from APMEX at Hanimaadhoo (MCO-H), Maldives-Gan (MCO-G; 0.7°S, 73.2°E), Nepal-GVR (NCO-G; 27.7°N, 85.3°E), Gosan (KCO-G; 33.3°N, 126.2°E), and Trinidad Head (NACO-T; 41.0°E, 124.3°W) [*Ramanathan et al., 2007*]. Data at Cape Hedo for the air mass from Korea/Japan, Pacific Ocean, and China [*Hatakeyama et al., 2005*]; Beijing data reported by *He et al.* [2004], *Duan et al.* [2006], *Chan et al.* [2005] and *Dan et al.* [2004] are also shown.

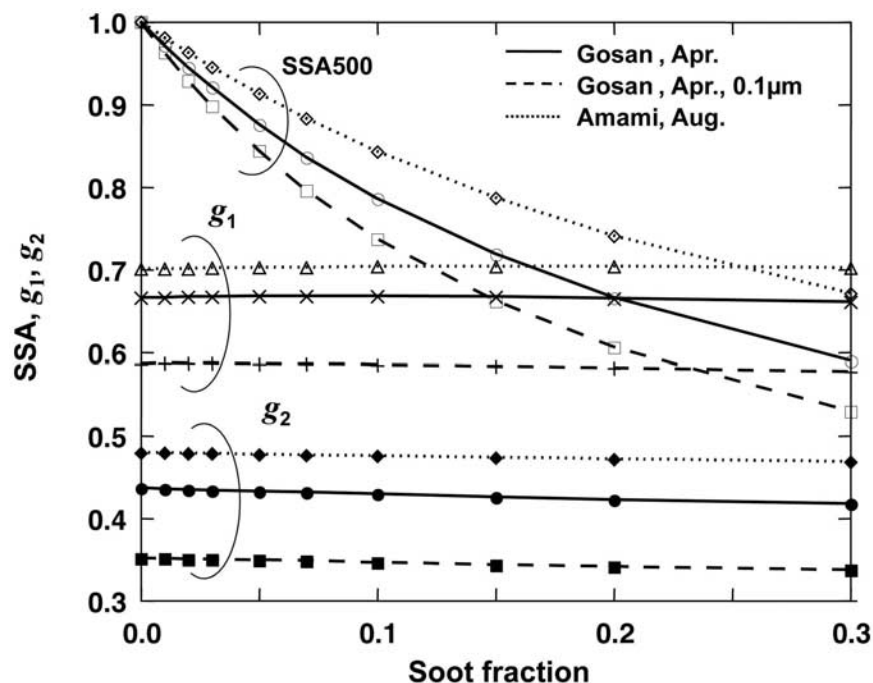


Figure 11. SSA500 and first two phase function moments of the fine aerosol mode, g_1 and g_2 , as a function of the volume soot fraction to the volume of the fine particle mode for three aerosol models: fine particle model aerosol polydispersions in the April atmospheric condition at Gosan and in the August condition at Amami for a lognormal volume size distribution with $r_m = 0.15 \mu\text{m}$. A case for Gosan condition with a reduced mode radius of $r_m = 0.1 \mu\text{m}$ is also shown.

where V_n , $r_{m,n}$, and σ_n represents the volume, mode radius, and log-dispersion of each aerosol mode ($n = 1$ for fine particle mode and $n = 2$ for dust particle mode).

[16] Figure 10 shows scatterplots of the measured elemental carbon (EC) mass fraction to the total carbonaceous aerosol mass (TC) at several sites of APMEX [Ramanathan *et al.*, 2007] and EAREX 2005. The fraction ranges from 5 to 30% with large values for the air mass transported from China as well as inside China. There is a tendency of getting a large EC/TC ratio as the TC increases. This tendency is different from that of Hanimadhoo site at which the EC/TC ratio can become high even when the TC is small. Since the ratio of TC to the aerosol mass changes in a large range from 20% to 70% if we include mineral dust aerosols at Gosan [Miyazaki *et al.*, 2007] and Amami [Nakajima *et al.*, 2003], the EC to total aerosol volume ratio can range from 1% to 20% in the EAREX region if we use the same density for these constituents. Figure 11 shows SSA500 and the first two moments of the aerosol phase function at $\lambda = 500 \text{ nm}$ (g_1 and g_2), assuming NCEP monthly mean atmospheric profiles in April at Gosan and in August at Amami as two largely different atmospheric conditions in the EAREX region. The mode radius and log-standard deviation for the fine particle mode are set as $r_1 = 0.15 \mu\text{m}$ and $\sigma_1 = 0.588$ as commonly observed values in the EAREX region as shown in Figure 12 by retrieved volume size distributions at the Gosan site. We also show results for a reduced particle mode radius of $r_1 = 0.1 \mu\text{m}$ for a case of a nearby emission source. Figure 12 shows SSA500 for fine particle mode aerosols can take a value as low as 0.5. The above mentioned range of EC/TC ratio from 1% to 20% suggests

that SSA500 can take values from 0.7 to 1.0, but it is possible for SSA500 to take a value as low as 0.6 at location near emission sources where the particle radius is generally small as $0.1 \mu\text{m}$. It is also found that the summer time tends to have large SSA values due to hygroscopic growth of aerosols absorbing water vapor. The water vapor effect also changes the phase function moments, whereas the soot fraction does not significantly change the moments.

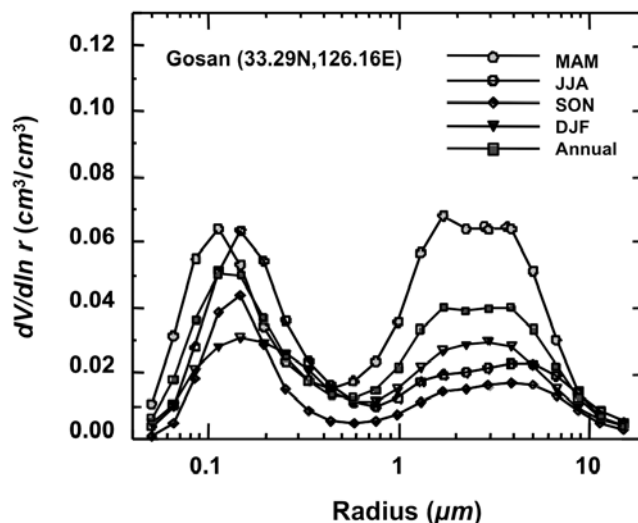


Figure 12. Volume size distributions observed at the Gosan site with an AERONET Sun/sky photometer. Data are from April 2001 to June 2006.

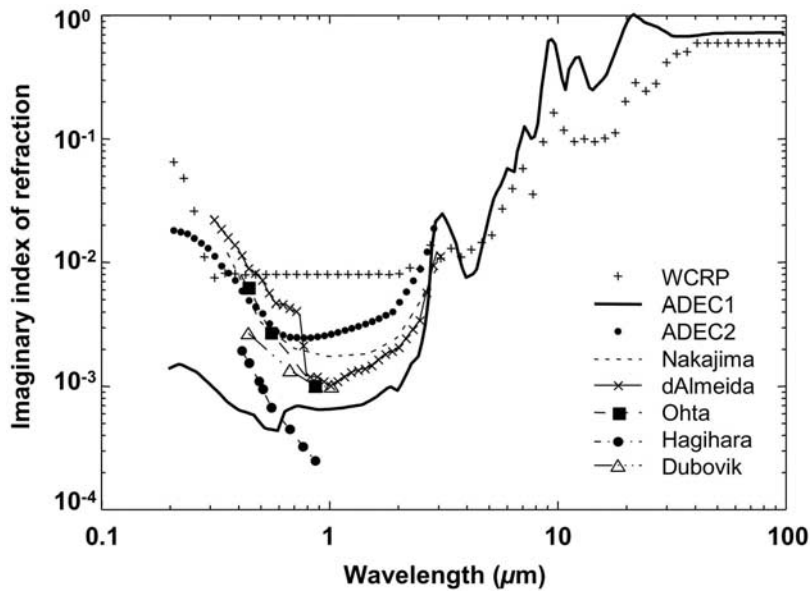


Figure 13. Spectra of the imaginary part of the refractive index of mineral dust aerosols from past studies: *Deepak and Gerber* [1983] (WCRP), *Aoki et al.* [2005] (ADEC1 and ADEC2), *Nakajima et al.* [1989] (Nakajima), *d’Almeida et al.* [1991], *Li et al.* [2003] (Ohta), *Hagihara et al.* [2006] (Hagihar), and *Dubovik et al.* [2002] (Dubovik).

[17] As for mineral dust aerosol, the effect of the imaginary index of refraction of mineral dust particles need to be studied because of large variation in the reported values [*Sokolik et al.*, 1998; *Kaufman et al.*, 2001]. We summarize several proposed spectra of the imaginary index of refraction as in Figure 13 in order to study the observed range of

the imaginary index. ADEC1 and ADEC2 are spectra proposed by *Aoki et al.* [2005]. ADEC1 is a weighted mean of the measured and archived imaginary index of several minerals and with the smallest magnitude in the visible spectral range as small as $k = 0.0005$. ADEC2 is an average of the ADEC1 and the mineral dust model in OPAC 3.1

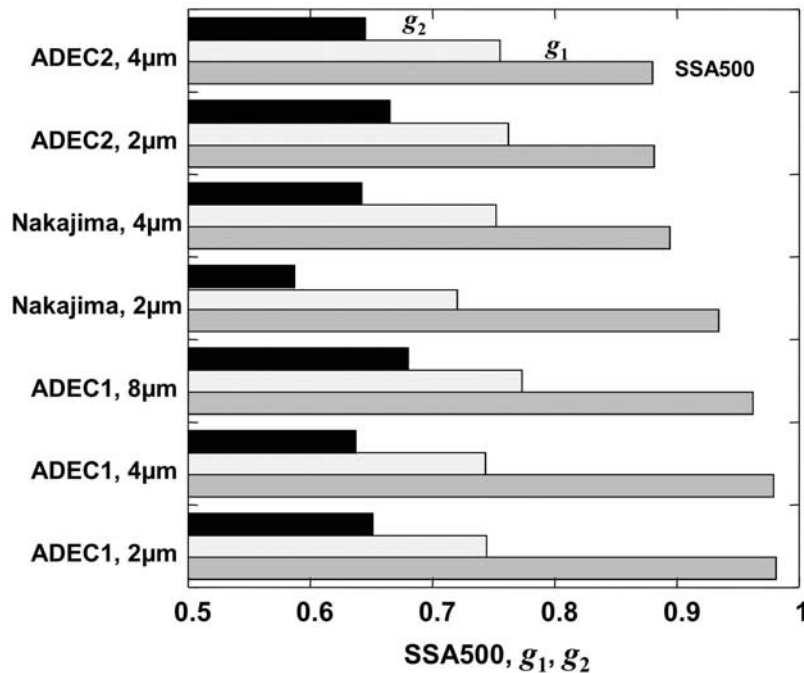


Figure 14. SSA500 and first two phase function moments of the coarse aerosol mode (g_1 and g_2) for different mode radii of the lognormal volume size distribution as $r_m = 2, 4, \text{ and } 8 \mu\text{m}$ and for different refractive index spectra of ADEC1, ADEC2 and Nakajima. The April monthly mean atmospheric condition at the Gosan site is assumed.

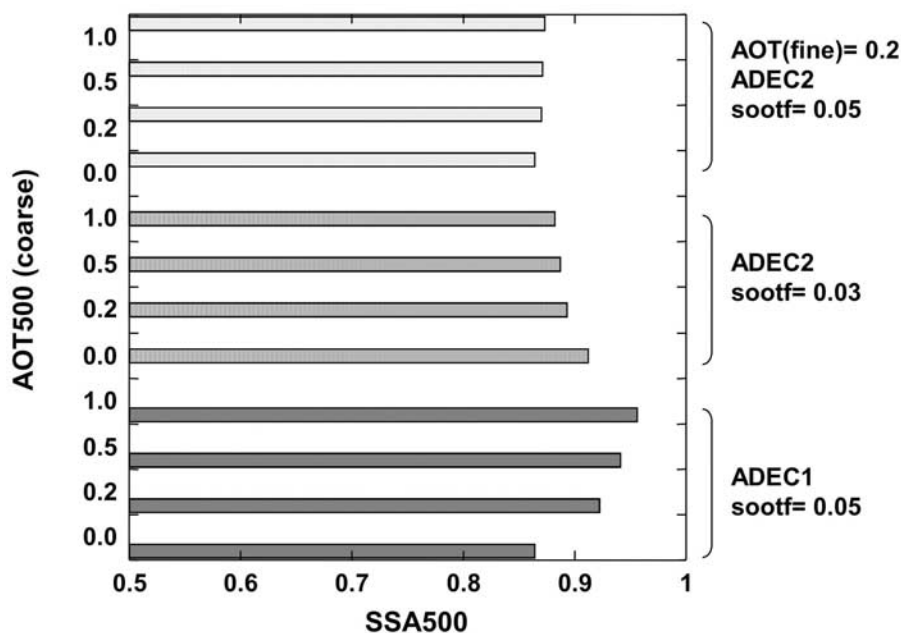


Figure 15. SSA500 for mixed aerosol polydispersions of fine and coarse aerosol modes. AOT500 for the fine mode is fixed at 0.2, while AOT500 for the coarse mode varies from 0 to 1. The soot fraction (sootf) of the fine mode is assumed to be 3% or 5%.

[Hess *et al.*, 1998]. The WCRP model is from the WCRP report [Deepak and Gerber, 1983]. Spectra from Nakajima *et al.* [1989] and d’Almeida *et al.* [1991] are also plotted. The Ohta model is a measurement of yellow sand from the Jinzhong basin of Shan Xi province by S. Ohta of Hokkaido University [Li *et al.*, 2003; S. Ohta, private communication, 1996]. This spectrum is close to the average of data from Bahrain and Solar Village obtained by Dubovik *et al.* [2002]. Hagihara *et al.* [2006] showed that SeaWiFS-observed radiances for Asian dust events can be explained when Ohta’s imaginary index k is reduced to $k/4$. Figure 13 shows that the ADEC1 and ADEC2 models cover the wide range of measured spectra, while Nakajima and d’Almeida spectra come in between these extremes. We therefore calculated SSA and the first two phase function moments at $\lambda = 500$ nm in Figure 14 with ADEC1, ADEC2 and Nakajima spectra. In the calculation we assumed the log dispersion of the coarse mode size distribution as $\sigma_2 = 1.10$ and various mode radii of 2, 4, and 8 μm to cover the range of observed mode radii in the EAREX region. The infrared part of the imaginary index and the whole spectrum of the real index of refraction of ADEC2 were set to be those of ADEC1, because this assumption does not significantly affect simulation results of ARF. Nonspherical scattering is calculated by the semiempirical theory of Pollack and Cuzzi [1980]. Figure 14 shows SSA500 can vary from 0.88 to 0.98 depending on the imaginary index spectra and mode radius of the coarse particle mode. For example the mode radius of the columnar volume spectrum measured by a sky radiometric technique changed from 2 μm to 10 μm depending on the transportation time of the air mass from 2 days from 5 days between Gobi Deserts to Nagasaki, Japan [Tanaka *et al.*, 1989]. Figure 14 indicates how the imaginary index of refraction and the particle radius have potential to change SSA in the dust event. It should be

recognized that the SSA500 value of absorbing fine particles in Figure 11 can come above or below the SSA500 value of the pure mineral dust particles shown in Figure 14, so that a dust loading into a fine particle system can increase or decrease the SSA value of the aerosol mixture. It is also found that the phase function moments show complicated changes depending on the refractive index model and the particle radius, especially for the ADEC1 model which has a small imaginary index of refraction to make the scattering efficiency factor sinusoidally oscillate as a function of particle size.

[18] Next we simulate SSA500 of external mixtures of fine particles and mineral dust particles as shown in Figure 15 for several values of AOT at 500 nm (AOT500) of mineral dust aerosols and two refractive index models of ADEC1 and ADEC2. The fine mode is assumed to include soot with 3% and 5% volume fractions. The AOT500 value of the fine mode is fixed at 0.2 as a representative value in the outflow region as shown in Figure 5. The ADEC1 mineral dust does not significantly absorb solar radiation, so that a loading of ADEC1 mineral dust particles increases SSA500 of the mixed air mass from 0.86 to 0.96. On the other hand, the ADEC2 mineral dust loading can either increase or decrease SSA depending on the soot fraction of the fine mode. The critical soot fraction at which dust loading does not change the SSA is between 3 to 5% in the case of the ADEC2 refractive index. It is found from Figure 15 that the SSA of a mixed polydispersion takes on a value in a relatively narrow range from 0.86 to 0.96 when the AOT500 of mineral dust aerosol is less than 0.2 which is the general situation common to both rural and urban situations in the EAREX region with absorbing aerosols loaded in the atmosphere [Tanaka *et al.*, 1983; Nakajima *et al.*, 1989, 2003; Kim *et al.*, 2004].

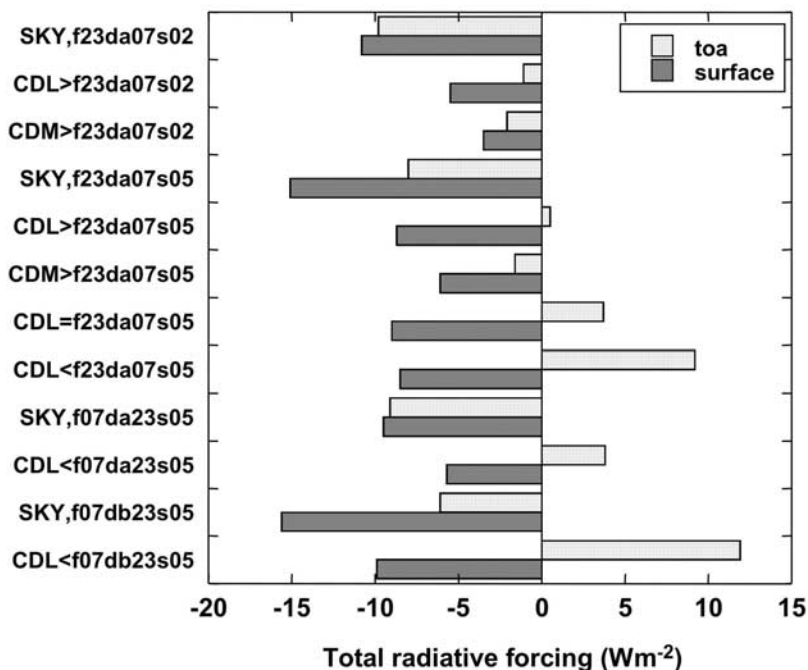


Figure 16. Total (SW + LW) aerosol radiative forcings (W m^{-2}) at TOA and surface for different aerosol polydispersions and vertical stratifications. Case keys are described in the caption of Table 4.

[19] For a sensitivity test, we computed the total ARF as in Figure 16 by taking the difference of net total, i.e., shortwave (SW) plus longwave (LW), radiation fluxes with and without aerosol loading at tropopause (we refer to this as TOA) and surface for different aerosol and cloud stratifications. In the computation the April 2005 monthly mean condition was assumed for the meteorological condition at the Gosan site using NCEP objective analysis data. Radiative transfer was solved by the *rstar-4.0b* radiation code of OpenCLASTR with a Lambertian surface condition of $A = 0.1$. The all-aerosol optical thickness at $\lambda = 500$ nm

(AOT500) is fixed at 0.3, which is close to the AOT averages shown in Figure 4. The optical thickness of the cloud layer is assumed to be 10 which is close to the mean value for each cloud type (low, middle, and high) at the six EAREX sites in March–April and September–October seasons. The aerosol size distribution is assumed to be $r_1 = 0.15 \mu\text{m}$ and $\sigma_1 = 0.18$ in equation (2). Table 4 summarizes aerosol parameters at $\lambda = 500$ nm and 865 nm, bottom and top heights of aerosol and cloud layers, and ARF values for total (SW + LW) and longwave radiation (LW). Figure 16 and Table 4 shows that the clear-sky total forcing for a light

Table 4. Aerosol Radiative Forcing Values (ARF) for the Total (SW+LW) Spectrum and the Longwave (LW) Spectrum^a

Stratification	Soot	Sootc	ARF(SW + LW)												aot500/ aot865	ssa500/ ssa865	g500/ g865	
			Fine			Dust			Cloud			toa		sfc				ARF(LW)
			aotf	btm	top	aotd	btm	top	cotw	btm	top	toa	sfc	toa	sfc	toa	sfc	
SKY,f23da07s2	2	–	0.23	0	1.0	0.07	0	1.0	–	–	–	–9.8	–10.8	–0.2	5.2	0.300/0.146	0.953/0.951	0.685/0.640
CDL > f23da07s2	2	–	0.23	0	1.0	0.07	0	1.0	10	1	1.5	–1.1	–5.5	0.0	0.1			
CDM > f23da07s2	2	–	0.23	0	1.0	0.07	0	1.0	10	4	5	–2.1	–3.5	0.0	1.7			
SKY,f23da7s5	5	–	0.23	0	1.0	0.07	0	1.0	–	–	–	–8.0	–15.1	–0.2	5.1	0.300/0.150	0.899/0.901	0.687/0.641
CDL > f23da7s5	5	–	0.23	0	1.0	0.07	0	1.0	10	1	1.5	0.5	–8.7	0.0	0.1			
CDM > f23da7s5	5	–	0.23	0	1.0	0.07	0	1.0	10	4	5	–1.6	–6.1	0.0	1.7			
CDL = f23da7s5	5	–	0.23	1	1.5	0.07	1	1.5	10	1	1.5	3.7	–9.0	0.0	0.1			
CDL < f23da7s5	5	–	0.23	2	3.0	0.07	2	3.0	10	1	1.5	9.2	–8.5	0.3	0.0			
SKY,f7da23s5	5	–	0.07	1	1.5	0.23	2	3	–	–	–	–9.1	–9.5	2.5	8.6	0.300/0.257	0.953/0.968	0.726/0.714
CDL < f7da23s5	5	–	0.07	2	3	0.23	2	3	10	1	1.5	3.8	–5.7	1.0	0.1			
SKY,f7db23s5	5	–	0.07	1	1.5	0.23	2	3	–	–	–	–6.1	–15.6	2.5	8.5	0.300/0.258	0.874/0.930	0.734/0.714
CDL < f7db23s5	5	–	0.07	2	3	0.23	2	3	10	1	1.5	11.9	–9.9	1	0.1			
SKY,f23da7s10	10	–	0.07	1	1.5	0.23	2	3	–	–	–	–8.5	–11.4	2.5	8.5	0.300/0.259	0.931/0.955	0.728/0.715
SKY,f23da7s10sc1	10	1	0.07	1	1.5	0.23	2	3	–	–	–	–3.8	–18.6	2.5	8.6	0.300/0.259	0.838/0.880	0.747/0.731
SKY,f23db7s10sc1	10	1	0.07	1	1.5	0.23	2	3	–	–	–	–2.4	–2.2	2.5	8.6	0.300/0.260	0.795/0.856	0.750/0.728

^aUnit is W m^{-2} . Stratification keys stand for cases of clear-sky (SKY), low-level cloud (CDL) and midlevel cloud (CDM) with an aerosol layer below (>), above (<) or within(=) the cloud layer; AOT500 for the fine aerosol mode of 0.07 (f7) or 0.23 (f23) with soot fraction (Soot) of 2% (s02), 5% (s05) and 10% (s10); AOT500 for the coarse particle mode of 0.07 with ADEC1 or ADEC2 models (da7 or db01) or of 0.3 (da03 or db03) with soot fraction (Sootc) of 0% (dashes) or 1% (sc1). Bottom and top heights of fine, dust and cloud layers are shown in columns labeled btm and top. AOT500 values for fine aerosol, dust aerosol and the cloud optical thickness value for water cloud are shown in columns labeled aotf, aotd and cotw. Values of AOT, SSA and g are listed in the last three columns labeled aot500, ssa500 and g500 for $\lambda = 500$ nm and aot865, ssa865 and g865 for 865 nm.

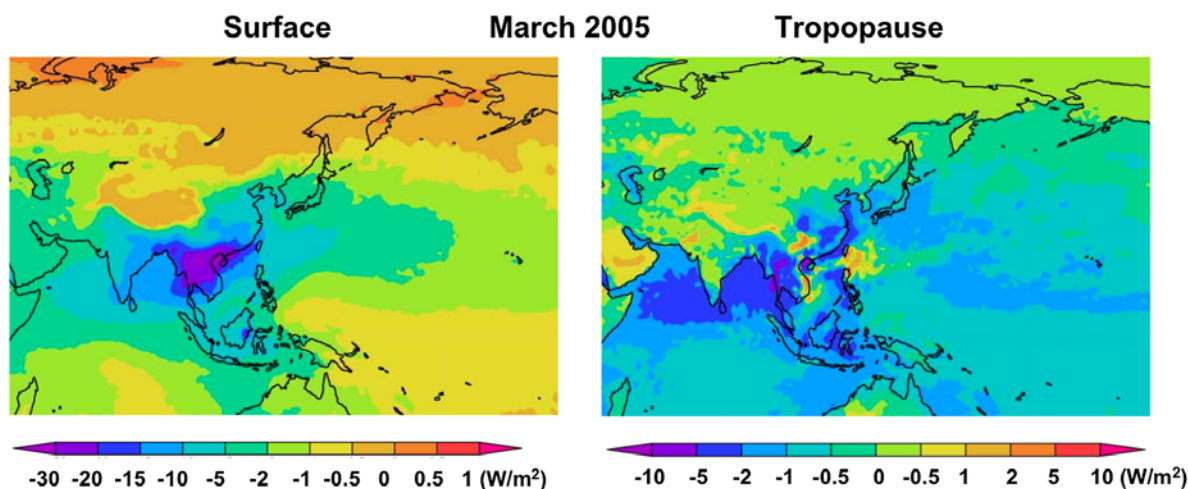


Figure 17. Total (SW + LW) aerosol radiative forcings (W m^{-2}) at TOA and surface in the APMEX and EAREX regions as simulated by the SPRINTARS model. Monthly mean values for whole-sky condition of March 2005 are presented.

soot-loading (2%) condition is about -10 W m^{-2} both at surface and at TOA when fine particles and mineral dust particles are externally mixed in the lower 1 km layer where the AOT500 of fine and dust aerosols is 0.23 and 0.07, respectively (case 1). In this case, SSA500 takes a value of 0.95 which is an average of the observed values shown in Figure 6 other than Hefei data. A large negative forcing at surface of about -15 W m^{-2} is gained in the case of absorbing aerosols with a volume soot content of 5% with a SSA500 value of 0.899 which is slightly larger than the lower limit of SSA range at the surface of the sites under study other than that of Hefei (case 4). The clear-sky surface forcing in the dust event condition ranges from -9 W m^{-2} to -16 W m^{-2} depending on the dust models, ADEC1 or ADEC2, with largely different SSA500 values of 0.953 and 0.874, respectively (case 9 and 11). Several earlier studies [Chuang *et al.*, 2003; Aoki *et al.*, 2005; Shi *et al.*, 2005] also suggested large differences in the radiative forcing of the mineral dust-laden system depending on the dust optical properties. In order to investigate large surface ARF cases, we added one clear-sky case with soot fraction of 10% with the ADEC1 model (case 13) and two clear-sky cases with ADEC1 and ADEC2 models internally mixed with soot of 1% volume fraction (case 14 and 15). The ARF value of case 14 reaches -18.6 W m^{-2} much larger in magnitude than -11.4 W m^{-2} of case 13. This indicates that the effect of light absorption by soot particles mixed with coarse particles is much more effective than those with fine particles to increase the magnitude of ARF because large-sized particles do not lose their AOT in longer wavelengths at which the solar insolation still has large radiative energy.

[20] The clear-sky total TOA forcing decreases from -9.8 W m^{-2} to -8.0 W m^{-2} because of absorption of solar radiation when the soot fraction increases from 2% to 5% (case 1 and 4). A similar forcing change from -9.1 W m^{-2} to -6.1 W m^{-2} is possible in dust-laden clear-sky conditions depending on the dust model (case 9 and 11). Different from the surface forcing, the TOA forcing changes its sign depending on the aerosol and cloud layer heights. It can become as large as $+9.2 \text{ W m}^{-2}$ to $+11.9 \text{ W m}^{-2}$ when

the aerosol layer above a low cloud has a soot fraction of 5% or the mineral dust model of ADEC2 (case 8 and 12). This suggests that the vertical stratification of aerosol and cloud layers has a large potential to introduce an uncertainty of several watt per square meter in the estimated ARF unless we know accurate stratification.

[21] Figure 16 and Table 4 show the LW surface forcing, ARF(LW), takes a value between 0 W m^{-2} and $+9 \text{ W m}^{-2}$ under the clear-sky condition. The LW forcing is as large as $+5.2 \text{ W m}^{-2}$ even when the AOT500 of dust aerosol is only 0.07 and mixed in the relatively low altitude (case 1), indicating a substantial greenhouse effect can be caused by dust particles. This point brings a serious problem in the forcing evaluation, because it is difficult to determine the dust AOT fraction to the total AOT in most surface radiation measurements.

[22] The surface forcing is reduced by half to 1/3 but not to zero even in an overcast cloud condition, indicating that a simple evaluation of the forcing by weighting the clear-sky forcing with the clear-sky fraction underestimates the magnitude of the total forcing for the whole-sky condition (stratifications labeled *CDL* and *CDM* in Table 4). It is interesting to see that the surface forcing does not change much even when aerosols are mixed in the cloud layer (case 7 and 8). Figure 16 shows that the surface forcing is more than -8 W m^{-2} , regardless of the cloud layer height other than the light soot-loading case.

[23] Figure 17 shows the model-simulated global distributions of the monthly mean total direct ARF for whole-sky condition of March 2005 calculated by the AGCM+SPRINTARS model. In the APMEX region, the model simulation suggests the whole-sky total ARF from -2 to -5 W m^{-2} at TOA and from -5 to -15 W m^{-2} at surface in the APMEX region, while it ranges from -1 to -2 W m^{-2} at TOA and from -2 to -10 W m^{-2} at surface of the EAREX region. Corresponding simulated AOT550 in the APMEX region is from 0.2 to 0.3 with SSA550 from 0.88 to 0.92 as shown in Figure 7, while AOT550 in the EAREX region ranges from 0.2 to 0.5 with SSA550 from 0.90 to 0.96. Thus the simulation suggests that APMEX region is slightly less turbid than the EAREX, but more absorptive as also

inferred from the soot fraction diagram shown in Figure 10. The low whole-sky ARF in the EAREX region as compared to the ARF in the APMEX is mainly caused by the large cloud fraction in the former region as discussed in the next section.

[24] On the other hand, *Nakajima et al.* [2003] got the April monthly mean total ARF of -7.1 W m^{-2} at TOA and -18.2 W m^{-2} at surface of Gosan, and -5.6 W m^{-2} at TOA and -15.8 W m^{-2} at surface of Amami, whereas *Ramanathan et al.* [2001a] proposed the whole-sky direct ARF of about 0 W m^{-2} at TOA and -14 W m^{-2} at surface as an average of January to April season. Taking into account the fact that the mean AOT500 was 0.40 for the APEX-E2 period in 2001 and 0.26 for the EAREX 2005 IFO period in 2005, these observed ARF values are consistent with the model simulation results shown in Figure 17, but with slightly larger values. One possible reason is an overestimation of the cloud amount in these regions by the model as discussed in the next section. Also it is difficult to simulate the forcing in the spring season because of the large variability in forcing (in both SW and LW spectral regions) due to different mixtures of fine and mineral dust particles as shown in Table 4. *Shi et al.* [2005] obtained forcings three times more forcing, i.e., as -6 W m^{-2} and -30 W m^{-2} for AOT550 around 0.2 in the EAREX region for a dust event of 2001.

5. Discussion and Conclusions

[25] Before concluding the paper, we like to discuss several points which are not fully discussed in the previous sections.

[26] The SW ARF is well approximated by the formulae of *Nakajima et al.* [2003]. With more numerical experiments of the SW radiative transfer, we found the following formulae are a better approximation to the 24 hour mean clear-sky net SW radiative forcings at surface and TOA,

$$ARF(SW, \text{clr}, \text{sfc}) = -\beta_{\text{sfc}}\tau \quad (3a)$$

$$ARF(SW, \text{clr}, \text{toa}) = -\beta_{\text{toa}}\tau \quad (3b)$$

$$\beta_{\text{sfc}} \approx C_{\text{sfc}}\{(1-A)[1-\omega(f-\nu g)]-\omega bA(1-2\nu)\}^\zeta \quad (3c)$$

$$\beta_{\text{toa}} \approx C_{\text{toa}}\{\omega(b+\nu g)-2A\left[1-\omega f-\left(1-\frac{1+2g}{2}\omega\right)\nu\right]\}^\zeta \quad (3d)$$

$$f = \frac{1+g}{2}, \quad b = \frac{1-g}{2} \quad (3e)$$

$$\nu = \frac{1}{2}\left(1-\sqrt{3}\langle\cos\theta_0\rangle_{\text{daytime}}\right) \quad (3f)$$

where A is the ground albedo; τ , ω , and g are respectively aerosol optical thickness (AOT), single scattering albedo

(SSA), and asymmetry factor ($g = g_1$) at an effective wavelength λ_e to approximate the broadband fluxes by one wavelength solutions. In this study we assume $\lambda_e = 700 \text{ nm}$ after comparison of the approximation with simulated broadband fluxes. The constant ν is the deviation of the daytime mean cosine of the solar zenith angle from the two stream Gaussian quadrature point ($= 1/\sqrt{3}$). C_{sfc} and C_{toa} are constants to be determined so as to adjust the two stream solutions at an effective wavelength to the broadband radiative fluxes depending on the location and time of observation. The exponent ζ is also introduced empirically to correct the small nonlinear effects of the broadband solution. In the present work, we found the following expression as a better approximation:

$$C_{\text{sfc}} = TSD/R^2, \quad C_{\text{toa}} = TC_{\text{sfc}}, \quad \text{and } \zeta = 1.12, \quad (4)$$

where S , D , and R are the solar constant (approximately 1370 W m^{-2}), daytime fraction of the day, and Earth-Sun distance in astronomical unit, respectively; T is the broadband transmissivity of the atmosphere without aerosols, but including molecular scattering and ozone and water vapor absorption. T is about 0.768 for the Gosan site in spring season. It should be noted that the extraterrestrial solar insolation flux is proportional to D^2 , but the aerosol forcing is proportional to D because of increasing scattering cross section for the slant solar light path. The coefficients β can be called the aerosol forcing efficiencies at surface and TOA at the effective wavelength and as noted as β_{700} . The efficiencies at a commonly used wavelength of 500 nm (or 550 nm) can be obtained through the following relation using the definition of β in equations (3a) and (3b):

$$\beta_{500} = \tau_{700}\beta_{700}/\tau_{500}, \quad (5)$$

where τ_{500} and τ_{700} are optical thicknesses at 500 nm and 700 nm (AOT500 and AOT700), respectively. Formulae (2) and (3) agree with exact solutions, a database of 43 cases with radiative transfer computation, within *rsmid* error of 2.8 W m^{-2} for β_{500} at surface ranging 70 W m^{-2} to 200 W m^{-2} and 2.2 W m^{-2} for β_{500} at TOA ranging -3 W m^{-2} to 40 W m^{-2} .

[27] The above formulae indicate the surface forcing is mainly controlled by AOT and $\Lambda_1 = 1 - \omega f$. Therefore we should discuss the consistency of the broadband flux measurements and in situ aerosol and sky radiometer measurements in the EAREX region. At the Gosan site, *Takamura et al.* [2007] obtained the mean clear-sky shortwave ARF from observations using a pyranometer and a sky radiometer as -8.0 W m^{-2} at TOA and -23.4 W m^{-2} at surface with AOT500 = 0.255 as mean values for the IFO period of EAREX 2005 (almost equinox condition; $D = 0.5$, $R1$, and $\nu = 0.038$). Corresponding efficiency factors are as large as $\beta_{\text{toa},500} = 31.5 \text{ W m}^{-2}$ and $\beta_{\text{srf},500} = 91.8 \text{ W m}^{-2}$. According to equations (3)–(5), the difference in the surface efficiency factor can be attributed to the change in the aerosol parameters through the following relation if the latitude of the site is not too high to change the ν value significantly and we put $\zeta = 1$ in the first-order approximation,

$$\delta\beta_{\text{sfc},500} = -C_{\text{sfc}}(1-A)\delta(\omega_{700}f_{700})\tau_{700}/\tau_{500}. \quad (6)$$

Table 5. Estimation of SSA700 (ω_{700}) From Observed ARF Efficiency Factors at 500 nm (β_{500}) Obtained by Clear-Sky Surface Broadband Flux Measurements at the Gosan Site: Nondust and Dust Cases of *Kim et al.* [2005] and EAREX 2005 Period Averages of *Takamura et al.* [2007]^a

Case	Stratification	Reference Model ^b				Kim, Nondust ^c			Kim, Dust ^c		Takamura ^d	
		τ_{700}	ω_{700}	g_{700}	β_{500} (Exact)	β_{500} (eq3)	ω_{700}	β_{500} (eq3)	ω_{700}	β_{500} (eq3)	ω_{700}	
1	SKY,f23da7s2	0.191	0.952	0.654	53.3	55.4	0.856	55.4	–	54.5	–	
4	SKY,f23da7s5	0.194	0.901	0.655	67.3	69.7	0.906	69.7	–	67.3	–	
9	SKY,f7da23s5	0.271	0.962	0.718	60.3	62.3	0.925	62.3	–	64.1	–	
11	SKY,f7db23s5	0.272	0.920	0.717	80.3	78.8	0.961	78.8	–	78.7	0.873	
13	SKY,f23da7s10	0.273	0.945	0.720	66.3	68.6	0.932	68.6	–	69.8	0.845	
14	SKY,f23da7s10sc1	0.273	0.864	0.736	90.7	96.9	–	96.9	0.824	94.9	0.860	
15	SKY,f23db7s10sc1	0.274	0.840	0.732	102.0	107.8	–	107.8	0.844	104.5	0.879	
Observation						69.0	0.920	104.0	0.840	91.8	–	

^aAlso listed are aerosol parameters at 500 nm (τ_{700} , ω_{700} and g_{700}), β_{500} for the reference models of Table 4 to be used in equation (6), ground albedo A and constants (D , R , T and ν) in equations (3) and (4).

^b $A = 0.1$, $D = 0.5$, $R = 1$, $T = 0.768$, and $\nu = 0.038$.

^c $A = 0.06$, $D = 0.534$, $R = 1$, $T = 0.768$, and $\nu = -0.002$.

^d $A = 0.1$, $D = 0.5$, $R = 1$, $T = 0.768$, and $\nu = 0.038$.

This equation makes it possible to estimate a SSA700 value to fit Takamura's observed value using the model parameters listed in Table 4. In order to translate the exact reference model values with full radiative transfer calculation in the equinox condition, $\beta_{500}(\text{exact, ref})$, to the observation condition we use equation (3),

$$\beta_{500}(\text{ref}) = \beta_{500}(\text{eq3, obs})\beta_{500}(\text{exact, ref})/\beta_{500}(\text{eq3, ref}), \quad (7)$$

where the exact reference value in the equinox condition is given as $\beta_{500}(\text{exact, ref}) = [\text{ARF}(\text{SW} + \text{LW}) - \text{ARF}(\text{LW})]/0.3$ from Table 4 and two approximate values, $\beta_{500}(\text{eq3, ref})$ for the reference condition and $\beta_{500}(\text{eq3, obs})$ for the observation condition, are calculated using equation (3). Table 5 summarizes these values with aerosol parameters at 700 nm. Estimated SSA700 are shown only when the difference between observed and reference efficiency factors is less than 15 W m^{-2} from the observed values. It is found SSA700 is around 0.86 without much dependence on the reference model used for estimation. The asymmetry factor takes a value larger than 0.7. Takamura et al. reported that the period-averaged Ångström exponent α was 0.92. Since there is a linear relation between the asymmetry factor g and the Ångström exponent α in the 43 cases database of radiative transfer simulation,

$$g_{700} = -0.079\alpha + 0.758, \quad (8)$$

we have an estimate of g_{700} as 0.685 for the Takamura's case, which is not too far from our estimate in Table 5. Such a large asymmetry factor suggests the Gosan atmosphere should have a significant coarse mode of dust particles and/or sea spray even in the normal condition without Asian dust events to produce enough large forcing at surface. Consistently, *Takamura et al.* [2007] claimed that lidar measurements at Gosan showed large signals from nonspherical coarse particles even in cases without significant Asian dust events. On the other hand, we have a problem of inconsistency with the sky radiometer measurements in Figure 6 which show a much larger SSA500 as 0.96. In this case, Table 5 indicates the efficiency factor should be as low as 60 W m^{-2} .

[28] *Kim et al.* [2005] also obtained the mean April 2001 efficiency factors using pyranometers and a sky radiometry at the Gosan site during the APEX-E2 ($D \cong 0.534$, $R \cong 1$, $\nu = -0.001$) as $\beta_{\text{toa},500} = -29 \text{ W m}^{-2}$ and $\beta_{\text{srf},500} = -69 \text{ W m}^{-2}$ for nondust condition and $\beta_{\text{toa},500} = -21 \text{ W m}^{-2}$ and $\beta_{\text{srf},500} = -104 \text{ W m}^{-2}$ for dust condition. These values seem to be consistent with the values obtained by *Yoon et al.* [2005] as $\beta_{\text{toa},500} = -30 \text{ W m}^{-2}$ and $\beta_{\text{srf},500} = -81 \text{ W m}^{-2}$ for an average of data in the spring season from 2001 to 2003. In their evaluation they used a surface albedo of $A = 0.06$ at Gosan obtained by the Surface Radiation Budget (SRB) data of the Atmospheric Sciences Data Center (NASA LaRC). Taking into account that asymmetry factors are reported as 0.69 in nondust case and 0.70 in dust case, Table 5 shows Kim's surface efficiency factors fit a SSA700 around 0.92 for the nondust condition and 0.83 for the dust condition. These values are consistent with Kim's study that SSA500 is 0.92 for nondust case and 0.84 for dust cases. Thus Kim's efficiency factor for the nondust case is consistent with the mean SSA values for the EAREX IFO period obtained in the present study and also with the mean April 2001 SSA500 of 0.93 obtained by *Nakajima et al.* [2003] at Gosan.

[29] On the other hand, Takamura's case and Kim's dust case need very small SSA value. *Nakajima et al.* [2003] found a significant decrease in SSA500 as low as 0.8 in the large dust event during 11 to 16 April 2001. In this regard we have to note that SSA values given by *Nakajima et al.* [2003, Figure 7] were obtained by a nephelometer and an absorption photometer with a sampling system of 50% cutoff at 1 micron radius. The contribution from mineral dust particles, therefore, is partial compared to all-aerosol cases. If this point is taken into account, Nakajima's result may be similar to the result of *Clarke et al.* [2004] who proposed that SSA of the fine aerosol mode decreased down to 0.75 with increasing coarse aerosol mass loading. Nonetheless, the column total SSA value from a sky radiometer analysis in the APEX-E2 case also showed a SSA time series similar to that of absorption photometer/nephelometer measurements with low SSA values close to 0.8 in the dust events. *Sohn et al.* [2007] also showed a time series of decreasing SSA down to 0.9 as a dust plume of 7 April 2000, which crossed the Beijing city, approached the

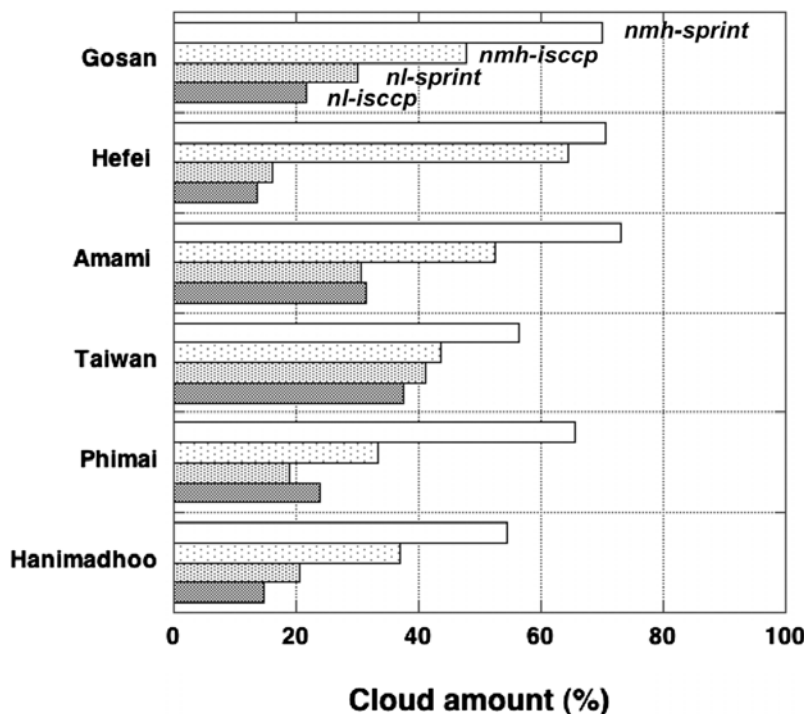


Figure 18. Cloud amounts of low-level clouds (*l*) and high-level clouds (*mh*) below and above 680 hPa, respectively, obtained from ISCCP statistics (*isccp*) and from the GCM (*sprint*). Bimonthly means for March and April are shown at six sites in the EAREX experiment.

observation site in Korea. These studies show that it is possible to have such small SSA values even for column total aerosols.

[30] Several reasons for the phenomenon of large ARF can be considered. Dust events tend to be associated with outflow of polluted air in the Asian countries, so that the SSA tends to be smaller than that of the dust event in Saharan dust storm cases. *Hatakeyama et al.* [2005] showed that EC content is much higher in the air mass from China as compared to those of Korea and Japan. In this regard, it is possible that transparent volatile materials can be adsorbed onto the surface of mineral dust aerosols to enhance the light absorption by soot particles [Tang *et al.*, 2004; Clarke *et al.*, 2004]. Hygroscopic growth is reduced in the dry air mass from the continent in the dust event to decrease the SSA value. We also cannot discard a possibility of the large imaginary index of mineral dust particles from different emission sources and local sources. Table 5 shows an introduction of the ADEC2 model can produce β_{700} larger than 78 (case 11). Another efficient way to increase the efficiency factor more than 90 is to include soot particles of 1% volume fraction with dust particles (case 14 and 15). In this case the ADEC1 model is enough to produce such large efficiency factor. *Chuang et al.* [2003] sampled Asian dust particles with strong absorption (SSA as low as 0.85) in the ACE-Asia case (same period as that of APEX-E2) and also a considerable amount of soot particles existed in radius range large than 1 micron, although they did not see a significant reduction of SSA when the strong absorption mineral dust particles are mixed with soot particles of 0.4% volume fraction which is the mean fraction of their measurements. It is also possible to have errors in instrumentations

and retrieval methods. We cannot identify what is the main reason for this phenomenon, because we did not have large-scale dust events in the EAREX campaign period. It is difficult to judge whether the dips in the SSA time series in Figure 6 corresponds to this phenomenon. Nonetheless we like to point out that mixture of fine and coarse particles and/or inclusion of soot particles on the surface of coarse particles can produce a strong effect on the SW and LW radiative forcing of aerosols.

[31] Another factor that introduces uncertainty to our analysis is the effect of cloud stratification and surface albedo. Figure 18 shows the mean cloud fraction of two months (March–April) for low-level clouds and high-level clouds below and above 680 hPa, respectively, as obtained by ISCCP cloud statistics [Rossow and Garder, 1993] and by the present GCM model at six ABC sites. The cloud fraction for high-level clouds in the present study includes that for midlevel clouds by the IPCC definition. Figure 18 shows the model overestimates the cloud fractions both for low and high clouds suggesting a model underestimation of the magnitude of ARF by 7% to 20% at all the sites. This point has been stated in the preceding section regarding Figure 17. Apart from this difference, both the satellite and the model indicate that the Gosan site has more clouds than the Hanimadhoo site, which yields a smaller ARF at Gosan than at Hanimadhoo even with the larger AOT as shown in Figure 7. This has also been pointed out in the preceding section. Note that the AOT at Phimai is large enough to cause positive forcing even though the cloud fraction in this region is also large (Figures 7 and 17). It is found from Figure 18 that Phimai, Hanimadhoo, and Amami have more high-level plus midlevel clouds than Hefei and Gosan,

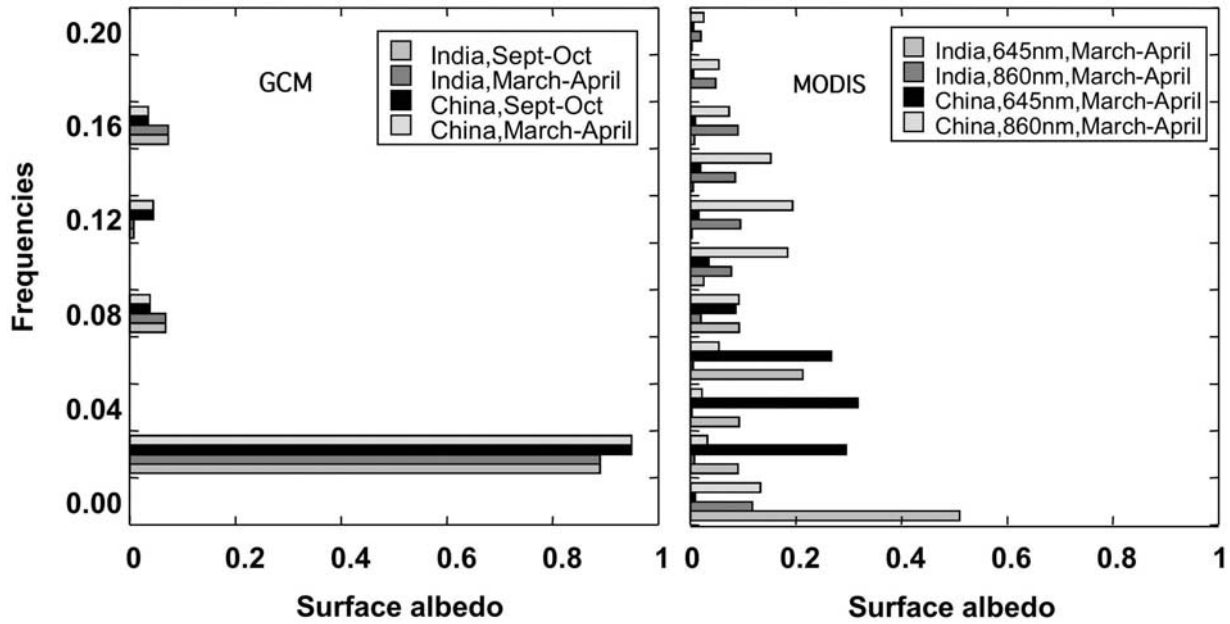


Figure 19. Ground albedo frequency distributions obtained from the GCM and from MODIS clear-sky radiance data for March 2005 after Rayleigh scattering correction at wavelengths of 645 nm and 860 nm.

indicating the atmosphere is deeper in terms of thermal stratification at southern sites than at northern sites as also indicated by the aerosol stratification in Figures 8 and 9. This is one of the reasons why the TOA forcing is larger in magnitude in the APMEX region than in the EAREX region as shown in Figure 17. There is a tendency to overestimate the high cloud amount by about 15% by the GCM common to all the sites, that will cause a underestimation of the aerosol forcing because it is not possible for aerosols to overlay the high cloud layer (above 440 hPa according to the ISCCP category) to reduce the TOA albedo of the Earth-atmosphere system. The cloud top height of low clouds is about 1.5 km in the IPCC statistics, while the aerosol layer scale height in EAREX region ranges from 1 km to 1.5 km as shown in Figure 9. This discussion leads to the conclusion that the TOA forcing may be biased toward the positive sign, i.e., the magnitude of the simulated forcing may be underestimated by the present GCM. The larger forcings measured by surface observations support this possibility.

[32] Equation (3) indicates that the TOA forcing depends on a combination of aerosol parameters and ground albedo approximately as $\Lambda_2 = \omega b - 2A(1 - \omega f)$, so that a special case of no ARF, i.e., $\Lambda_2 = 0$, can happen when absorbing aerosols lie over a high albedo surface or a cloud layer [Fraser and Kaufman, 1985]. This suggests that we have to investigate the adequacy of ground surface albedo values in our model calculation. Figure 19 shows bimonthly mean histograms (March to April 2005) of the surface albedo for solar radiation obtained from either SPRINTARS simulations and MODIS satellite observation for two regions, i.e., the APMEX area including India with longitude and latitude range (10–25°N, 65–90°E), and the EAREX area including China (20–40°N, 105–120°E). The MODIS observation were made at two wavelengths of 645 nm and 860 nm around the red-edge of vegetation reflection. In Figure 19 we see that the GCM modeling simulates the general

features of the surface conditions producing a large albedo over arid region and vegetation region, but in a highly simplified way, and on average we see an underestimation of the surface albedo. We performed a radiative transfer computation for calculating the clear-sky shortwave radiative forcing with various values of the ground albedo and weighted the albedo probability distributions given in Figure 19 from MODIS observation and model simulation. We confirm that the surface albedo effect by equation (3) can give a good approximation to the detailed transfer calculation result, which can be expressed as follows:

$$\begin{aligned} \delta(\text{ARF}, A) &\approx -\tau_a \delta \int_0^1 \beta_{\text{toa}}(A) f(A) dA \\ &= \frac{2C_{\text{toa}} T^2 SD(1 - \omega f) \tau_a}{R^2} \delta \langle A \rangle, \end{aligned} \quad (9)$$

when a spatially homogeneous aerosol layer exists above the Earth's surface with various surface albedo, where the bracket symbol, $\langle \rangle$, represents of area average operation. For an aerosol layer with AOT500 of 0.3 for fine particles and 0.1 for dust particles assuming the ADEC1 dust model, giving SSA500 = 0.906 and $g = 0.691$, the radiative transfer computation gives the uncertainty in the clear-sky shortwave aerosol forcing as -2.4 W m^{-2} , respectively, when the surface albedo differs as shown in Figure 19. This amount of uncertainty is not so significant for the area mean forcing over the Chinese region (20–40°N, 105–120°E) including the ocean region for the March–April season which is -10.1 W m^{-2} as was estimated with the MODIS-derived albedo probability distribution. However, the uncertainty becomes significant if we restrict the area to the land area of surface albedo larger than 10% where the forcing becomes about -6.0 W m^{-2} .

Table 6. Uncertainties in Parameter Values Met in EAREX 2005 and Rough Estimates of the Whole-Sky Aerosol Forcing Error Δ ARF Caused by the Uncertainties

Parameters	Accuracy	Δ ARF, $W m^{-2}$	Issues
AOT700	0.05	2.4	cloud screening
SSA700	0.05	3.0	large differences among model, sky radiometry, and flux measurements; larger SSA at Gosan than at Amami, but no simulation of this tendency by model results; soot fraction in coarse particle mode; large ARF cases of dust storms
g700	0.03	1.9	Ångström exponent measurement important; large impact on both SW and LW fluxes
Scale height	500 m	?	aerosols above low cloud layer and hygroscopic growth effects important
Ground albedo	0.02	2.4	poor model evaluation
Water vapor	0.05 in T	1.7	each profile at observation site needed
Solar geometry	3 in β_{500}	1.0	one month difference not negligible
High-level cloud fraction	0.15	1.5	model values not suitable

[33] In conclusion the present study elucidated the characteristic features of aerosols and the radiation budget in the EAREX 2005 experiment. Time series of AOT, SSA as well as lidar and CO concentration have shown that air pollutants and mineral dust were transported every 5 to 7 days in the experimental region to produce SSA700 values from 0.86 to 0.96 and large clear-sky shortwave forcing efficiency at 500 nm from $60 W m^{-2}$ to $90 W m^{-2}$, though there were some unexplained inconsistencies depending on the evaluation method. The simulated whole-sky total forcing in the EAREX region is from -1 to $-2 W m^{-2}$ at TOA and -2 to $-10 W m^{-2}$ at the surface which is smaller in magnitude than those of the APMEX region, mainly because of large cloud fraction in this region, though we have suggested there may be an underestimation of the forcing due to overestimation of the simulated cloudiness and aerosol scale height. On the other hand the possible error in the simulated surface albedo may cause an overestimation of the magnitude of the forcing over the land area.

[34] In order to make a better understanding of aerosol role to the radiation budget in Asia, we need more detailed analysis of the model and observation comparison to confirm these points and to find the reason why we have such an inconsistency. Finally we summarize in Table 6 the uncertainties in the whole-sky aerosol radiative forcing caused by uncertainties in each parameter studied in this work. Table 6 indicates unlucky combination of several factors can produce a large error in the forcing evaluation. Especially it is important to note the effects from SSA and asymmetry factor are larger than the uncertainty caused by uncertainty in AOT. We need to narrow these uncertainties in the future works. We also want to emphasize that intensive studies of the optical properties of mixed air mass of anthropogenic pollutants and mineral dust are especially needed.

[35] **Acknowledgments.** This research was supported by Global Environment Research Fund B-4 of Ministry of Environment Japan; RR2002 project and the data integration for Earth Observation Project of Ministry of Science, Sports, and Culture; and the JAXA/ADEOS-II GLI project. S.-C. Yoon was supported by the Korea Foundation for International Cooperation of Science and Technology (KICOS) through a grant provided by the Korean Ministry of Science and Technology (MOST) M60501000073-05A0100-07310 and by the Climate Environment System Research Center sponsored by the SRC program of Korea Science and Engineering Foundation. We are grateful to the Korean Meteorological Agency for operation of the Gosan supersite and the EAREX 2005 campaign support. Zhanqing Li and Can Lin of the University of Maryland is greatly acknowledged for providing us with the Xianghe CO data in Figure 2. We used ISCCP data sets and NASA MODIS aerosol retrieval data. Maki Yamano is greatly acknowledged for her technical support of this work.

References

- Aoki, T., T. Y. Tanaka, A. Uchiyama, M. Chiba, M. Mikami, and S. Yabuki (2005), Sensitivity experiments of direct radiative forcing caused by mineral dust simulated with a chemical transport model, *J. Meteorol. Soc. Jpn.*, *83A*, 315–331.
- Chan, C. Y., X. D. Xu, Y. S. Li, K. H. Wong, G. A. Ding, L. Y. Chan, and X. H. Cheng (2005), Characteristics of vertical profiles and sources of PM_{2.5}, PM₁₀ and carbonaceous species in Beijing, *Atmos. Environ.*, *139*, 5113–5124.
- Chuang, P. Y., R. M. Duvall, M. S. Bae, A. Jefferson, J. J. Schauer, H. Yang, J. Z. Yu, and J. Kim (2003), Observations of elemental carbon and absorption during ACE-Asia and implications for aerosol radiative properties and climate forcing, *J. Geophys. Res.*, *108*(D23), 8634, doi:10.1029/2002JD003254.
- Clarke, A. D., et al. (2004), Size distributions and mixtures of dust and black carbon aerosol in Asian outflow: Physicochemistry and optical properties, *J. Geophys. Res.*, *109*, D15S09, doi:10.1029/2003JD004378.
- d'Almeida, G. A., P. Koepke, and E. P. Shettle (1991), *Atmospheric Aerosols: Global Climatology and Radiative Characteristics*, A. Deepak, Hampton, Va.
- Dan, M., G. Zhuang, X. Li, H. Tao, and Y. Zhuang (2004), The characteristics of carbonaceous species and their sources of PM_{2.5} in Beijing, *Atmos. Environ.*, *38*, 3443–3452.
- Deepak, A., and H. E. Gerber (Eds.) (1983), Report of the experts meeting on aerosols and their climatic effects, *Rep. WCP-55*, World Clim. Res. Programme, Geneva, Switzerland.
- Duan, F. K., K. B. He, Y. L. Ma, F. M. Yang, X. C. Yu, S. H. Cadle, T. Chan, and P. A. Mulawa (2006), Concentration and chemical characteristics of PM_{2.5} in Beijing, China: 2001–2002, *Sci. Total Environ.*, *355*, 264–275.
- Dubovik, O., B. Holben, T. F. Eck, A. Smirnov, Y. J. Kaufman, M. D. King, D. Tanré, and I. Slutsker (2002), Variability of absorption and optical properties of key aerosol types observed in worldwide locations, *J. Atmos. Sci.*, *59*, 590–608.
- Fraser, R. S., and Y. J. Kaufman (1985), The relative importance of aerosol scattering and absorption in remote sensing, *IEEE Trans. Geosci. Remote Sens.*, *GE-23*, 625–633.
- Hagihara, Y., H. Fukushima, I. Uno, and S. Ohta (2006), Evaluation of Asian dust absorption in visible band with satellite observation, sky-radiometer measurements, and chemical transport model, *Sci. Online Lett. Atmos.*, *2*, 120–123, doi:10.2151/sola.2006-031.
- Hatakeyama, S., T. Imai, T. Miyoshi, and A. Takami (2005), Establishment of Japanese super site, Cape Hedo Atmosphere and Aerosol Monitoring Station (CHAAMS), and measurements of EC/OC at Cape Hedo in 2004, paper presented at 12th National Conference on Atmospheric Environment, Chin. Soc. for Environ. Sci., Dandong, China, Oct.
- Hayasaka, T., S. Satake, A. Shimizu, N. Sugimoto, I. Matsui, K. Aoki, and Y. Muraji (2007), Vertical distribution and optical properties of aerosols observed over Japan during Atmospheric Brown Clouds-East Asia Regional Experiment 2005, *J. Geophys. Res.*, *112*, D22S35, doi:10.1029/2006JD008086.
- Haywood, J., and O. Boucher (2000), Estimates of the direct and indirect radiative forcing due to tropospheric aerosols: A review, *Rev. Geophys.*, *38*, 513–543.
- He, Z., Y. J. Kim, K. O. Ogunjobi, J. E. Kim, and S. Y. Ryu (2004), Carbonaceous aerosol characteristics of PM_{2.5} particles in Northeastern Asia in summer 2002, *Atmos. Environ.*, *38*, 1795–1800.
- Hess, M., P. Koepke, and I. Schult (1998), Optical properties of aerosols and clouds: The software package OPAC, *Bull. Am. Meteorol. Soc.*, *79*, 831–844.

- Higurashi, A., and T. Nakajima (2002), Detection of aerosol types over the East China Sea near Japan from four-channel satellite data, *Geophys. Res. Lett.*, *29*(17), 1836, doi:10.1029/2002GL015357.
- Holben, B. N., et al. (2001), An emerging ground-based aerosol climatology: Aerosol optical depth from AERONET, *J. Geophys. Res.*, *106*, 12,067–12,097.
- Huebert, B. T., T. Bates, P. B. Russell, G. Y. Shi, Y. J. Kim, K. Kawamura, G. Carmichael, and T. Nakajima (2003), An overview of ACE-Asia: Strategies for quantifying the relationships between Asian aerosols and their climatic impacts, *J. Geophys. Res.*, *108*(D23), 8633, doi:10.1029/2003JD003550.
- Jacob, D. J., J. H. Crawford, M. M. Kleb, V. E. Connors, R. J. Bendura, J. L. Raper, G. W. Sachse, and J. C. Gille (2003), The Transport and Chemical Evolution over the Pacific (TRACE-P) aircraft mission: Design, execution, and first results, *J. Geophys. Res.*, *108*(D20), 9000, doi:10.1029/2002JD003276.
- Kaufman, Y. J., D. Tanré, O. Dubovik, A. Karnieli, and L. A. Remer (2001), Absorption of sunlight by dust as inferred from satellite and ground-based remote sensing, *Geophys. Res. Lett.*, *28*, 1479–1482.
- Kaufman, Y. J., D. Tanré, and O. Boucher (2002), A satellite view of aerosols in the climate system, *Nature*, *419*, 215–223.
- Kim, D.-H., B.-J. Sohn, T. Nakajima, T. Takamura, T. Takemura, B.-C. Choi, and S.-C. Yoon (2004), Aerosol optical properties over east Asia determined from ground-based sky radiation measurements, *J. Geophys. Res.*, *109*, D02209, doi:10.1029/2003JD003387.
- Kim, D.-H., B.-J. Sohn, T. Nakajima, and T. Takamura (2005), Aerosol radiative forcing over East Asia determined from ground-based solar radiation measurements, *J. Geophys. Res.*, *110*, D10S22, doi:10.1029/2004JD004678.
- Kondo, Y., et al. (2004), Photochemistry of ozone over the western Pacific from winter to spring, *J. Geophys. Res.*, *109*, D23S02, doi:10.1029/2004JD004871.
- Li, C., L. T. Marufu, R. R. Dickerson, Z. Li, T. Wen, Y. Wang, P. Wang, H. Chen, and J. W. Stehr (2007), In-situ measurements of trace gases and aerosol optical properties at a rural site in northern China during East Asian Study of Tropospheric Aerosols: An International Regional Experiment 2005, *J. Geophys. Res.*, *112*, D22S04, doi:10.1029/2006JD007592.
- Li, L., H. Fukushima, R. Frouin, B. G. Mitchell, M. He, I. Uno, T. Takamura, and S. Ohta (2003), Influence of submicron absorptive aerosol on Sea-viewing Wide Field-of-view Sensor (SeaWiFS)-derived marine reflectance during Aerosol Characterization Experiment (ACE)-Asia, *J. Geophys. Res.*, *108*(D15), 4472, doi:10.1029/2002JD002776.
- Li, Z., et al. (2007), Preface to special section on East Asian Studies of Tropospheric Aerosols: An International Regional Experiment (EAST-AIRE), *J. Geophys. Res.*, *112*, D22S00, doi:10.1029/2007JD008853.
- Mikami, M., G. Y. Shi, I. Uno, S. Yabuki, Y. Iwasaka, M. Yasui, T. Aoki, T. Y. Tanaka, Y. Kurosaki, and K. Masuda (2006), Aeolian dust experiment on climate impact: An overview of Japan-China joint project ADEC, *Global Planet. Change*, *52*, 142–172.
- Miyazaki, Y., Y. Kondo, S. Han, M. Koike, D. Komada, H. Tanimoto, and H. Matsueda (2007), Chemical characteristics of water-soluble organic carbon in the Asian outflow, *J. Geophys. Res.*, *112*, D22S30, doi:10.1029/2007JD009116.
- Nakajima, T., and S.-C. Yoon (Eds.) (2005), Implementation plan for ABC Gosan Campaign: East Asia Regional Experiment 2005, 73 pp., Sch. of Earth and Environ. Sci., Seoul Natl. Univ., Seoul, South Korea.
- Nakajima, T., M. Tanaka, M. Yamano, M. Shiobara, K. Arao, and Y. Nakanishi (1989), Aerosol optical characteristics in the yellow sand events observed in May, 1982 in Nagasaki—Part II: Model, *J. Meteorol. Soc. Jpn.*, *67*, 279–291.
- Nakajima, T., G. Tonna, R. Rao, Y. Kaufman, and B. Holben (1996), Use of sky brightness measurements from ground for remote sensing of particulate polydispersions, *Appl. Opt.*, *35*, 2672–2686.
- Nakajima, T., et al. (2003), Significance of direct and indirect radiative forcings of aerosols in the East China Sea region, *J. Geophys. Res.*, *108*(D23), 8658, doi:10.1029/2002JD003261.
- Pollack, J. B., and J. N. Cuzzi (1980), Scattering by non-spherical particles of size comparable to a wavelength: A new semi-empirical theory and its application to tropospheric aerosols, *J. Atmos. Sci.*, *37*, 868–881.
- Ramana, M. V., and V. Ramanathan (2006), Abrupt transition from Natural to anthropogenic aerosol radiative forcing: Observations at the ABC-Maldives Climate Observatory, *J. Geophys. Res.*, *111*, D20207, doi:10.1029/2006JD007063.
- Ramanathan, V., and P. J. Crutzen (2003), New directions: Atmospheric brown clouds, *Atmos. Environ.*, *37*, 4033–4035.
- Ramanathan, V., P. J. Crutzen, J. T. Kiehl, and D. Rosenfeld (2001a), Aerosols, climate, and the hydrological cycle, *Science*, *294*, 2119–2124.
- Ramanathan, V., et al. (2001b), Indian Ocean Experiment: An integrated analysis of the climate forcing and effects of the great Indo-Asian haze, *J. Geophys. Res.*, *106*, 28,371–28,398.
- Ramanathan, V., et al. (2007), Atmospheric brown clouds: Hemispherical and regional variations in long range transport, absorption and radiative forcing, *J. Geophys. Res.*, *112*, D22S21, doi:10.1029/2006JD008124.
- Rossow, W. B., and L. C. Garder (1993), Cloud detection using satellite measurements of infrared and visible radiances for ISCCP, *J. Clim.*, *6*, 2341–2369.
- Satheesh, S. K., and J. Srinivasan (2002), Enhanced aerosol loading over Arabian Sea during the pre-monsoon season: Natural or anthropogenic?, *Geophys. Res. Lett.*, *29*(18), 1874, doi:10.1029/2002GL015687.
- Sawa, Y., et al. (2007), Widespread pollution events of carbon monoxide observed over the western North Pacific during the East Asian Regional Experiment (EAREX) 2005 campaign, *J. Geophys. Res.*, *112*, D22S26, doi:10.1029/2006JD008055.
- Shi, G. Y., H. Wang, B. Wang, W. Li, S. Gong, and T. Zhao (2005), Sensitivity experiments on the effects of optical properties of dust aerosols on their radiative forcing under clear sky condition, *J. Meteorol. Soc. Jpn.*, *83A*, 333–346.
- Sohn, B.-J., T. Nakajima, H.-W. Chun, and K. Aoki (2007), More absorbing dust aerosol inferred from sky radiometer measurements at Anmyeon, Korea, *J. Meteorol. Soc. Jpn.*, in press.
- Sokolik, I. N., O. B. Toon, and R. W. Bergstrom (1998), Modeling the radiative characteristics of airborne mineral aerosols at infrared wavelengths, *J. Geophys. Res.*, *103*, 8813–8826.
- Stone, A. E., G. C. Lough, J. Schauer, P. Siva, C. Corrigan, and V. Ramanathan (2007), Understanding the origin of black carbon in the atmospheric brown cloud over the Indian Ocean, *J. Geophys. Res.*, *112*, D22S23, doi:10.1029/2006JD008118.
- Sugimoto, N., and C. H. Lee (2006), Characteristics of dust aerosols inferred from lidar depolarization measurements at two wavelengths, *Appl. Opt.*, *45*, 7468–7474.
- Takamura, T., N. Sugimoto, A. Shimizu, A. Uchiyama, A. Yamazaki, K. Aoki, T. Nakajima, B. J. Sohn, and H. Takenaka (2007), Aerosol radiative characteristics at Gosan, Korea, during the Atmospheric Brown Cloud East Asian Regional Experiment 2005, *J. Geophys. Res.*, *112*, D22S36, doi:10.1029/2007JD008506.
- Takemura, T., H. Okamoto, Y. Maruyama, A. Numaguti, A. Higurashi, and T. Nakajima (2000), Global three-dimensional simulation of aerosol optical thickness distribution of various origins, *J. Geophys. Res.*, *105*, 17,853–17,873.
- Takemura, T., T. Nakajima, O. Dubovik, B. N. Holben, and S. Kinne (2002), Single scattering albedo and radiative forcing of various aerosol species with a global three-dimensional model, *J. Clim.*, *15*, 333–352.
- Takemura, T., T. Nakajima, A. Higurashi, S. Ohta, and N. Sugimoto (2003), Aerosol distributions and radiative forcing over the Asian-Pacific region simulated by Spectral Radiation-Transport Model for Aerosol Species (SPRINTARS), *J. Geophys. Res.*, *108*(D23), 8659, doi:10.1029/2002JD003210.
- Takemura, T., T. Nozawa, S. Emori, T. Y. Nakajima, and T. Nakajima (2005), Simulation of climate response to aerosol direct and indirect effects with aerosol transport-radiation model, *J. Geophys. Res.*, *110*, D02202, doi:10.1029/2004JD005029.
- Tanaka, M., T. Takamura, and T. Nakajima (1983), Refractive index and size distribution of aerosols as estimated from light scattering measurements, *J. Clim. Appl. Meteorol.*, *22*, 1253–1261.
- Tanaka, M., T. Nakajima, M. Shiobara, M. Yamano, and K. Arao (1989), Aerosol optical characteristics in the yellow sand events observed in May, 1982 in Nagasaki—Part I: Observation, *J. Meteorol. Soc. Jpn.*, *67*, 267–278.
- Tang, Y., et al. (2004), Impacts of dust on regional tropospheric chemistry during the ACE-Asia experiment: A model study with observations, *J. Geophys. Res.*, *109*, D19S21, doi:10.1029/2003JD003806.
- Tanimoto, H., et al. (2007a), Direct assessment of international consistency of standards for ground-level ozone: Strategy and implementation toward metrological traceability network in Asia, *J. Environ. Monit.*, *9*, 1183–1193.
- Tanimoto, H., et al. (2007b), Evaluation of standards and methods for continuous measurements of carbon monoxide at ground-based sites in Asia, *Pap. Meteorol. Geophys.*, *58*, 85–93.
- Uchiyama, A., A. Yamazaki, K. Matsuse, and E. Kobayashi (2007), Broad-band shortwave calibration results for East Asia Regional Experiment 2005, *J. Geophys. Res.*, *112*, D22S34, doi:10.1029/2006JD008110.
- Uno, I., H. Amano, S. Emori, K. Kinoshita, I. Matsui, and N. Sugimoto (2001), Trans-Pacific yellow sand transport observed in April 1998: A numerical simulation, *J. Geophys. Res.*, *106*(D16), 18,331–18,344.
- Uno, I., G. R. Carmichael, D. Streets, S. Satake, T. Takemura, J. Woo, M. Uematsu, and S. Ohta (2003a), Analysis of surface black carbon distributions during ACE-Asia using a regional-scale aerosol model, *J. Geophys. Res.*, *108*(D23), 8636, doi:10.1029/2002JD003252.
- Uno, I., et al. (2003b), Regional chemical weather forecasting system CFORS: Model descriptions and analysis of surface observations at

- Japanese island stations during the ACE-Asia experiment, *J. Geophys. Res.*, 108(D23), 8668, doi:10.1029/2002JD002845.
- Uno, I., et al. (2004), Numerical study of Asian dust transport during the springtime of 2001 simulated with the Chemical Weather Forecasting System (CFORS) model, *J. Geophys. Res.*, 109, D19S24, doi:10.1029/2003JD004222.
- Won, J.-G., S.-C. Yoon, S.-W. Kim, A. Jefferson, E. G. Dutton, and B. Holben (2004), Estimation of direct radiative forcing of Asian dust aerosols with Sun/sky radiometer and lidar measurement at Gosan, Korea, *J. Meteorol. Soc. Jpn.*, 82, 115–130.
- Yoon, S.-C., J.-G. Won, A. H. Omar, S.-W. Kim, and B.-J. Sohn (2005), Estimation of the radiative forcing by key aerosol types in worldwide locations using a column model and AERONET data, *Atmos. Environ.*, 39, 6620–6630.
-
- K. Aoki, Department of Earth Science, Faculty of Sciences, University of Toyama, Toyama 930-8555, Japan.
- D. Goto, T. Nakajima, N. Schutgens, and H. Tsuruta, Center for Climate System Research, University of Tokyo, Room 206, General Research Building, 5-1-5 Kashiwanoha, Kashiwa, Chiba 277-8568, Japan. (teruyuki@ccsr.u-tokyo.ac.jp)
- A. Higurashi, A. Shimizu, N. Sugimoto, and H. Tanimoto, Atmospheric Environment Division, National Institute for Environmental Studies, Tsukuba, Ibaraki 305-8506, Japan.
- S.-W. Kim, B.-J. Sohn, and S.-C. Yoon, School of Earth and Environmental Sciences, Seoul National University, Seoul 151-742, South Korea.
- C.-T. Lee, Graduate Institute of Environmental Engineering, National Central University, Chungli 32001, Taiwan.
- N.-H. Lin, Department of Atmospheric Sciences, National Central University, Chungli 320, Taiwan.
- V. Ramanathan, Scripps Institution of Oceanography, University of California, San Diego, La Jolla, CA 92093, USA.
- Y. Sawa, Geochemical Research Department, Meteorological Research Institute, Tsukuba, Ibaraki 305-0052, Japan.
- G.-Y. Shi, Institute of Atmospheric Physics, Beijing 100029, China.
- T. Takamura, Center for Environmental Remote Sensing, Chiba University, Chiba 263-8522, Japan.
- T. Takemura, Research Institute for Applied Mechanics, Kyushu University, Kasuga, Fukuoka 816-8580, Japan.